Zeitschrift: Helvetica Physica Acta
Band: 61 (1988)
Heft: 8

Artikel: Spin dynamics of transitions among muon states in semiconductors
Autor: Odermatt, W.
DOI: https://doi.org/10.5169/seals-115984

Helvetica Physica Acta, Vol. 61 (1988) 1087–1129 0018–0238/88/081087–43$1.50 + 0.20/0

Spin dynamics of transitions among muon states in semiconductors

By W. Odermatt

Physik-Institut, Universität Zürich, 8001 Zürich, Switzerland

(26. III. 1988)

Abstract. The muon spin rotation (μSR) technique was used to study muonium centers in the elemental semiconductors diamond and silicon, and the compounds CuCl, CuBr and CuI. In diamond, the thermally-activated transition from the isotropic muonium state Mu to the anisotropic muonium state Mu* is used to determine the sign of the Mu* hyperfine constants. It is found that the isotropic part of the Mu* hyperfine interaction is *negative* presumably due to exchange polarization, supporting the bond-center model for Mu*. Two isotropic muonium states, Mu^{I} and Mu^{II}, are observed at low temperatures in CuCl and CuBr, and a diamagnetic 'bare' muon state (μ^+) is seen at high temperature. A study was made of the irreversible $Mu^{I} \rightarrow Mu^{II} \rightarrow \mu^+$ transitions in CuCl. Several unusual properties of these muonium centers in the copper halides, when compared with Mu in other tetrahedrally coordinated materials, will be discussed. The low-temperature Mu and Mu* states in high-purity silicon both become unstable at higher temperature, undergoing irreversible transitions to the μ^+ state. At the highest temperatures investigated, even this μ^+ state becomes unstable, indicating *reversible* transitions of the type $\mu^+ \leftrightarrow$ Mu. A generalized theory which treats the time-dependent muon polarization during transitions among various muon states is presented and applied to the situations mentioned above.

I. Introduction

A positive muon implanted into an insulator or a semiconductor may bind an electron to form a muonium (μ^+e^-) atom. Since the muon mass is approximately $\frac{1}{9}$ of the proton mass, muonium may be considered a light isotope of hydrogen [1]. Properties of muonium and hydrogen in vacuum are compared in Table 1. It is expected that these two atoms will remain electronically similar when implanted into a solid. In contrast to the case of hydrogen, which has not been observed in a paramagnetic state in semiconductors, two different muonium states have been observed in semiconductors: i) normal muonium (Mu), which is characterized by a strong isotropic hyperfine (*hf*) interaction, and ii) anomalous muonium (Mu*), characterized by a weak axially symmetric *hf* interaction. Such muonium states can be studied with the muon-spin-rotation (μSR) method [3, 4]. In this technique, polarized positive muons (μ^+) are stopped in the material to be investigated, and the time-dependent muon polarization is monitored via positrons from the anisotropic muon-decay which are recorded as a function of the elapsed time since a muon stop.

The spin Hamiltonian for normal muonium, which describes the *hf*

Table 1
Comparison of hydrogen and muonium in vacuum from Ref. 2.

	H	Mu
Mass (m_e)	1837.15	207.769
Reduced electron mass (m_e)	0.999456	0.995187
Ground-state radius a (Å)	0.529465	0.531736
Ground-state energy (eV)	−13.5984	−13.5403
Nuclear gyromagnetic ratio γ ($s^{-1}T^{-1}$)	2.67520×10^8	8.51607×10^8
Hyperfine frequency A (MHz)	1420.41	4463.30

interaction in an external field $\vec{B}$ can be written:

$$\mathcal{H} = hA\vec{I} \cdot \vec{S} - g_\mu \mu_\mu \vec{I} \cdot \vec{B} - g_e \mu_B \vec{S} \cdot \vec{B} \tag{1}$$

where $\vec{I}$ and $\vec{S}$ are the muon and electron spin operators and A is the *hf* frequency, which is proportional to the electron density at the muon site [2, 5]:

$$A = -\frac{2}{3h} \mu_0 g_e g_\mu \mu_B \mu_\mu |\Psi(0)|^2 \tag{2}$$

The energy-level diagram for normal muonium is shown in Fig. 1. In an external magnetic field transverse to the initial muon polarization, the indicated $\Delta m = \pm 1$ transitions are observed. For Mu in vacuum, $A_{vac} = 4463$ MHz, but in semiconductors and insulators A is in generally much smaller.

In the semiconductors diamond [2] silicon [6, 7], germanium [8], GaP and GaAs [9], an additional muonium state, Mu*, is observed whose *hf* interaction has ⟨111⟩-axial symmetry. The *hf* interaction of Mu* is strongly anisotropic, with

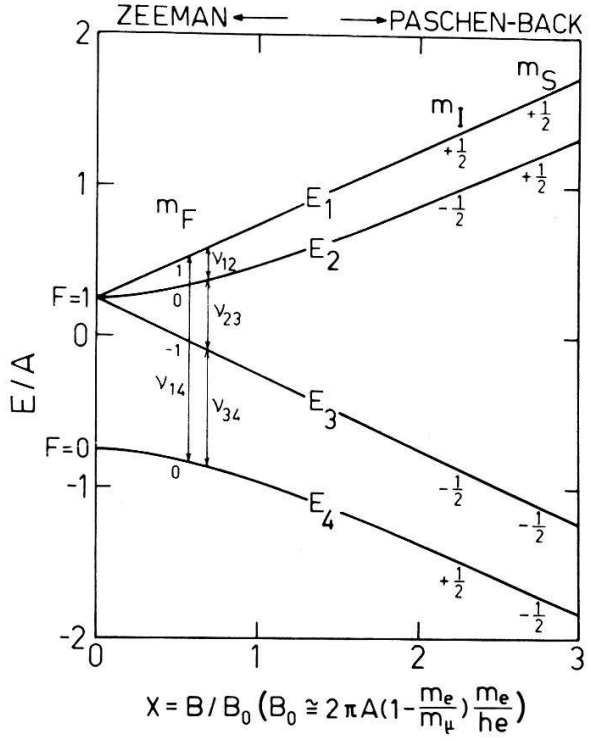

Figure 1
Energy-level diagram for normal muonium (Mu). The magnetic field X is measured in units of B_0. In vacuum, $B_0(\text{vac}) = 0.15868$ T. The transitions indicated corresponds to the observable μSR frequencies in a transverse field.

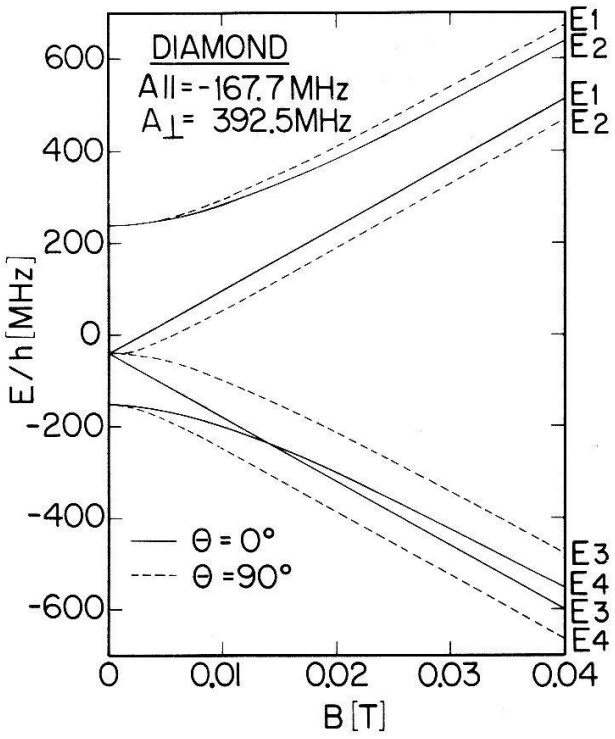

Figure 2
Energy-level diagram for anomalous muonium (Mu*) in diamond. The eigenvalues of the spin Hamiltonian (equation (3)) depend on the angle Θ between the symmetry axis $\vec{n}$ and the magnetic field $\vec{B}$.

coupling constants more than one order of magnitude weaker than that of vacuum Mu. The anisotropic spin Hamiltonian for Mu* has the form:

$$\mathcal{H} = hA_\perp \vec{I}\cdot\vec{S} + h(A_\parallel - A_\perp)(\vec{I}\cdot\vec{n})(\vec{S}\cdot\vec{n}) - g_\mu\mu_\mu \vec{I}\cdot\vec{B} - g_e\mu_B\vec{S}\cdot\vec{B} \qquad (3)$$

Here $\vec{n}$ is a unit vector along one of the four equivalent $\langle 111\rangle$ axes in the diamond lattice. Figure 2 gives the energy-level diagram for Mu* in diamond, using the hyperfine constants from Ref. 2. The anisotropy of the Mu* *hf* interaction implies that it is immobile in the host lattice. It is convenient to express the Mu* *hf* parameters in terms of the isotropic and anisotropic contributions [10] A_s and A_p, or in terms of ω_0 and ω^* as in [11]:

$$\begin{aligned} A_\perp &= A_s - A_p = \frac{1}{2\pi}\omega_0 \\ A_\parallel &= A_s + 2A_p = \frac{1}{2\pi}(\omega_0 + \omega^*) \end{aligned} \qquad (4)$$

The measured low-temperature *hf* parameters for all muonium states known in the diamond and zincblende semiconductors are summarized in Table 2.

An outstanding problem regarding Mu* is the *sign* of the *hf* coupling constants A_s and A_p defined in equations (3, 4). Since the electron spin density at the muon is reflected by A_s, knowledge of its sign is required in order to construct a realistic model of Mu*. For example, a positive spin density might indicate that a single paramagnetic electron occupies an orbital which is centered on the muon, while a negative spin density suggests that initially diamagnetic electrons at the muon are polarized by a more distant paramagnetic electron due to an exchange

Table 2
Low-temperature hyperfine parameters for anisotropic Mu* ($A_{\parallel}$, $A_{\perp}$) and isotropic Mu (A) in diamond and zincblende semiconductors, the maximum temperatures of their observation and observed transitions among the muon states. Beside some minor corrections the values are taken from Refs. 3, 12.

Sample	$A_{\parallel}$ (MHz)	$A_{\perp}$ (MHz)	A (MHz)	$T^{max}_{Mu^*}$ (K)	T^{max}_{Mu} (K)	Transitions
C	+167.983(57)	−392.586(55)	3711(21)	≥1000	405	$Mu \rightarrow Mu^*$
Si	16.819(11)	92.59(5)	2006.3(2.0)	165	300	$Mu^* \rightarrow \mu^+$
						$Mu \leftrightarrow \mu^+$
Ge	27.269(13)	131.037(34)	2359.5(2)	85	120	$(Mu, Mu^*) \rightarrow \mu^+$
β-SiC				≥22		$\mu^+ \rightarrow Mu$?
GaP	219.0(2)	79.48(7)	2914(5)	100	240	
GaAs	217.8(2)	87.74(6)	2883.6(3)	100	300	$Mu^* \rightarrow \mu^+$
ZnS			3547.8(3)		≥10	
ZnSe			3456.7(3)		≥13	
CuCl			$1334.24(7)^{I}$		60^{I}	$Mu^{I} \rightarrow Mu^{II}$
			$1212.75(12)^{II}$		445^{II}	$Mu^{II} \rightarrow \mu^+$
CuBr			$1403.70(7)^{I}$		153^{I}	$Mu^{I} \rightarrow Mu^{II}$
			$1250.79(22)^{II}$		$\geq 300^{II}$	$Mu^{II} \rightarrow \mu^+$?
CuI			1670.94(23)		102	

interaction. In a standard μSR experiment only the relative sign of A_s and A_p can be determined.

In diamond, zero-field measurements of the temperature-dependent Mu* signal strength in a powder sample demonstrated that a thermally-activated transition occurs from the Mu to the Mu* state [2]. Soon after this observation, Meier [11] suggested that single crystal measurements would show a resonant transfer of the muon polarization at particular applied magnetic fields where the Mu and Mu* precession frequencies coincide, and that such a resonance could be used to determine the sign of the Mu* hyperfine parameters. Such a measurement was attempted [13], but the sample was rich in nitrogen (type Ia), and rapid Mu relaxation, presumably due to impurity trapping, prevented a conclusive sign determination. In the present work, a nitrogen-*poor* stone (type IIb) was used, resulting in narrow precession lines and a sharp resonance. Furthermore, the elimination of Mu-trapping allowed us to follow the transition from the decay of the precursor Mu state to the enhancement of the Mu* signal strength, and to describe both processes with a single Arrhenius law. The large temperature region over which Mu signals could be observed in this sample (up to 400 K) also permitted a measurement of the temperature-dependence of the Mu *hf* frequency. A preliminary report of these experiments has been presented elsewhere [14].

Not only Mu in diamond, but *all* muonium states observed to date in semiconductors become unstable above a certain temperature T^{max} (see Table 2). At sufficiently high temperatures, only the precession of 'naked muons' (μ^+) in a diamagnetic environment is observed. Low-temperature μSR measurements in the group I–VII semiconductors [15] CuCl, CuBr and CuI reveal Mu centers with

weak isotropic *hf* parameters, approximately $\frac{1}{3}$ the vacuum value A_{vac}. In CuBr and CuCl two distinct Mu centers (Mu^I and Mu^{II}) are observed at low temperatures, whereas in CuI only one Mu center was observed. The temperature dependence of their *hf* coupling constants displays unusual characteristics when compared with the other semiconductors.

In a further experiment, the thermally-activated transitions $Mu^I \rightarrow Mu^{II} \rightarrow \mu^+$ in CuCl have been investigated. In addition, a search was made in CuCl for effects on the μSR spectra of the structural phase transition [16] from zincblende to wurtzite at 680 K and upon melting at 733 K.

Above room temperature, measurements on high-purity silicon show several interesting features: with increasing temperature, first the Mu signals disappear, then the μ^+ signal becomes stronger. At still higher temperatures the μ^+ depolarization rate increases as well. All the data for Mu and for μ^+ can be described consistently by a $Mu \leftrightarrow \mu^+$ transition model. The predicted μ^+ frequency shift for high transition rates is in good agreement with the observations.

The behavior of the muon polarization during irreversible transitions among muonium states has been described for several simple cases [11, 17–19]. These treatments are insufficient, however, for the more complex transitions seen in CuCl and Si. Here we develop a more generalized theory suggested by Celio [20]. Besides being capable of describing reversible transitions for an arbitrary number of muon states, this theory treats the effect of loss and conservation of the muonium electron polarization during the transition and allows the inclusion of a phenomenological electron spin depolarization of the type discussed by Ivanter and Smilga [17]. This generalized theory permits a consistent description of the experimental data.

The Paper is organized as follows: In Section II we present the generalized theory describing transitions among muon states. The experimental technique and sample-specific details are given in Section III. In Sections IV, V and VI, the experiments performed on diamond, the cuprous halides and silicon are presented. Conclusions are presented in Section VII.

II. Theory

In this Section we develop a general theoretical model suggested by Celio [20] which adequately describes the transitions among muon states which are of interest in this paper. In our discussion of the individual muon states, only the Mu* case is considered, since Mu and μ^+ are described by the same spin Hamiltonian (equation (3)) with different *hf* parameter values. To simplify the expressions, we follow the notation of [11], where the Mu* *hf* parameters ω_0 and ω^* are used. Introducing the vectors

$$\begin{aligned} \vec{\omega}_e &= \gamma_e \vec{B} = 2\pi \cdot 28024.21\ \mathrm{MHz}/T \times \vec{B} \\ \vec{\omega}_\mu &= \gamma_\mu \vec{B} = 2\pi \cdot 135.53\ \mathrm{MHz}/T \times \vec{B} \end{aligned} \tag{5}$$

and expressing the spin operators with the Pauli matrices σ and τ for the muon and the electron respectively, the Mu* spin Hamiltonian (3) can be rewritten:

$$\mathcal{H} = \tfrac{1}{4}\hbar\omega_0\vec{\sigma}\cdot\vec{\tau} + \tfrac{1}{4}\hbar\omega^*(\vec{\sigma}\cdot\vec{n})(\vec{\tau}\cdot\vec{n}) - \tfrac{1}{2}\hbar\vec{\omega}_\mu\vec{\sigma} + \tfrac{1}{2}\hbar\vec{\omega}_e\vec{\tau} \tag{6}$$

The g-factors in the muon and electron gyromagnetic ratios $\gamma_i = g_i\mu_i/\hbar$ are taken to be isotropic. The spin Hamiltonians for the individual muon states are obtained from equation (6) as follows:

$$\begin{aligned} &\text{Mu}^*\text{:}\quad \omega_0 \neq 0, \quad \omega^* \neq 0 \\ &\text{Mu:}\quad\ \omega_0 \neq 0, \quad \omega^* = 0 \\ &\mu^+\text{:}\quad\ \omega_0 = \omega^* = \omega_e = 0 \end{aligned} \tag{7}$$

(a) *The time-dependent muon polarization in the* Mu* *state*

The general density matrix for the two-particle system muon-electron is given by

$$\rho = \tfrac{1}{4}(1 + \vec{p}_\mu\cdot\vec{\sigma} + \vec{p}_e\cdot\vec{\tau} + p^{jk}\sigma_j\tau_k). \tag{8}$$

where

$$\begin{aligned} \vec{p}_\mu &= \mathrm{Tr}\,(\rho\vec{\sigma}) \\ \vec{p}_e &= \mathrm{Tr}\,(\rho\vec{\tau}) \\ p^{jk} &= \mathrm{Tr}\,(\rho\sigma_j\tau_k) \end{aligned} \tag{9}$$

are the muon, electron and mixed polarizations. Using the commutation relations

$$\begin{aligned} [\sigma_j, \sigma_k] &= 2i\epsilon_{jkl}\sigma_l \\ [\sigma_j\tau_m, \sigma_k\tau_n] &= 2i(\delta_{jk}\epsilon_{mnr}\tau_r + \delta_{mn}\epsilon_{jkl}\sigma_l) \end{aligned} \tag{10}$$

the equation of motion for the density matrix ρ

$$i\hbar\frac{d\rho}{dt} = [\mathcal{H}, \rho] \tag{11}$$

leads to the following set of 15 coupled differential equations for the polarizations

$$\begin{aligned} \dot{p}^j_\mu &= \epsilon_{jkl}\left[\frac{\omega_0}{2}p^{lk} + \frac{\omega^*}{2}n_k n_m p^{lm} - \omega^k_\mu p^l_\mu\right] \\ \dot{p}^j_e &= \epsilon_{jkl}\left[\frac{\omega_0}{2}p^{kl} + \frac{\omega^*}{2}n_k n_m p^{ml} + \omega^k_e p^l_e\right] \\ \dot{p}^{jk} &= \epsilon_{nlm}\left[\delta_{jm}\,\delta_{kn}\frac{\omega_0}{2}(p^l_\mu - p^l_e) - \delta_{jn}\left(\frac{\omega^*}{2}n_m n_k p^l_\mu - \omega^m_\mu p^{lk}\right)\right. \\ &\quad \left. + \delta_{kn}\left(\frac{\omega^*}{2}n_j n_l p^m_e + \omega^l_e p^{jm}\right)\right] \end{aligned} \tag{12}$$

describing the time evolution in the undisturbed Mu* state. With the vector

$$\vec{P} = \begin{pmatrix} \vec{p}_\mu \\ \vec{p}_e \\ p^{jk} \end{pmatrix} \tag{13}$$

this set of equations may be written as

$$\dot{P}_\alpha = M_{\alpha\beta} \cdot P_\beta \tag{14}$$

If U denotes the unitary matrix which diagonalizes $M(U^{-1}MU = D)$, we obtain

$$P_\alpha(t) = U_{\alpha n} U^{-1}_{n\beta} P_\beta(0) \exp(D_{nn} t) \tag{15}$$

where U and M are 15×15 matrices. For an undisturbed state, the purely imaginary elements of the eigenvector matrix D are oscillation frequencies. For later reference, equation (15) may be rewritten as:

$$\vec{P}(t) = \exp(Mt) \cdot \vec{P}(0) \tag{16}$$

The disturbance represented by an exchange of spin between the bound electron and the surroundings can be taken into account by adding to the right-hand side of equation (12) relaxation terms of the form

$$\begin{aligned} \dot{p}^j_e &= \cdots - 2\nu_{ex} \cdot p^j_e \\ \dot{p}^{jk} &= \cdots - 2\nu_{ex} \cdot p^{jk} \end{aligned} \tag{17}$$

where for the moment ν_{ex} is a phenomenological spin exchange rate. Such a disturbance has been studied in [17] and [21].

This set of equations can in certain cases be reduced. The muon polarization in the Mu* state depends on three vectors: (i) the direction of the external field $\vec{B}$ (taken to be the z axis), (ii) the unit vector $\vec{n}$ parallel to one of the four equivalent $\langle 111 \rangle$ directions in the crystal and (iii) the initial beam polarization $\vec{p}_\mu(0)$. The system of equation (12) and (17) can be separated into two subsystems, if $\vec{n} \perp \vec{B}$ or $\vec{n} \parallel \vec{B}$. One subsystem involves only the component of the muon and the electron polarizations along the magnetic field (longitudinal subsystem), and the other contains only the perpendicular components (transverse subsystem). For the isotropic state Mu, such a separation into subsystems is always possible [17, 22].

In the Appendix, reduced sets of coupled differential equations are summarized for $\vec{n} \perp \vec{B}$ and $\vec{n} \parallel \vec{B}$ for the longitudinal and transverse subsystems.

(b) *Spin dynamics of transitions among muon states*

In the investigated systems, the muon polarization may be carried over from one state to another (see Table 2). We are now concerned with the transformation of a state described by the spin Hamiltonian $\mathcal{H}_1$ (equation (6)) into a state described by the Hamiltonian $\mathcal{H}_2$ which has the same form but different *hf* parameters. Such a transformation is denoted by $\mathcal{H}_1 \rightarrow \mathcal{H}_2$. We assume that

$\mathcal{H}_1 \rightarrow \mathcal{H}_2$ occurs with the rate Λ_{12}, and we include the possibility of the inverse process $\mathcal{H}_2 \rightarrow \mathcal{H}_1$ with the rate Λ_{21}. Consider first the case where the electron polarization is conserved during the transitions. This is a reasonable assumption in view of ESR experiments on radical termination reactions [23].

Celio [20] has suggested an elegant method to treat such transformations. The total polarization in state 1 at time t is given by (i) those muonium atoms which are in state 1 at time zero and remain there until time t, plus (ii) the muonium atoms which undergo a transition from $2 \rightarrow 1$ at time $t' < t$, plus (iii) two transitions $(1 \rightarrow 2 \rightarrow 1)$, etc:

$$\begin{aligned}\vec{P}_1(t) = {} & \exp[(M_1 - \Lambda_{12})t] \cdot \vec{P}_1(0) \\ & + \Lambda_{21} \int_0^t dt' \exp[(M_1 - \Lambda_{12}) \cdot (t - t')] \exp[(M_2 - \Lambda_{21})t'] \cdot \vec{P}_2(0) \\ & + \Lambda_{12}\Lambda_{21} \int_0^t dt' \int_0^{t'} dt'' \exp[(M_1 - \Lambda_{12}) \cdot (t - t')] \\ & \times \exp[(M_2 - \Lambda_{21}) \cdot (t' - t'')] \exp[(M_1 - \Lambda_{12})t''] \cdot \vec{P}_1(0) \\ & + \cdots \end{aligned} \tag{18}$$

The same holds for $\vec{P}_2(t)$, which is obtained by exchanging the indices 1 and 2. The *total* polarization $\vec{P}^{\text{tot}}(t)$ is given by the sum:

$$\vec{P}^{\text{tot}}(t) = \vec{P}_1(t) + \vec{P}_2(t) \tag{19}$$

For the special case where only one jump is considered ($\Lambda_{21} = 0$) we regain the expressions obtained by Percival and Fischer [18] and by Meier [11].

The integral expressions in equation (18) are equivalent to the following set of two coupled differential equations

$$\begin{pmatrix} \dot{\vec{P}}_1 \\ \dot{\vec{P}}_2 \end{pmatrix} = \begin{pmatrix} M_1 - \Lambda_{12} & \Lambda_{21} \\ \Lambda_{12} & M_2 - \Lambda_{21} \end{pmatrix} \cdot \begin{pmatrix} \vec{P}_1 \\ \vec{P}_2 \end{pmatrix} \tag{20}$$

Note that the matrices M_1 and M_2 in equation (20) determine the polarization evolution in the individual states 1 and 2 and that the 'off-diagonal' terms Λ_{12} and Λ_{21} are responsible for the polarization transfer.

The loss of the electron polarization during the transition may thus be introduced by multiplying these off-diagonal terms by a matrix $\mathcal{A}$

$$\begin{aligned} \mathcal{A}_{ij} &= \delta_{ij} \quad \text{if } i, j = 1, 2, 3 \\ \mathcal{A}_{ij} &= 0 \quad \text{if } i, j = 4 \cdots 15 \end{aligned} \tag{20}$$

This prevents the electron polarization from being carried over from one state to the other. If the polarization is conserved in the transition, matrix $\mathcal{A}$ is the 15×15 unity matrix.

Consider now the special case where two identical states are involved ($M_1 = M_2 = M$), where both transformation rates are equal ($\Lambda_{12} = \Lambda_{21} = \Lambda$) and where the electron polarization is lost during the transition. The equations of

motion for the time-dependent polarizations are then given by:

$$\dot{\vec{P}}^{\text{tot}} = [M - \Lambda \cdot (1 - \mathcal{A})] \cdot \vec{P}^{\text{tot}} \tag{22}$$

This is exactly the same expression as equation (17). The rate ν_{ex} assumes the meaning of a transition rate for a muon jumping between equivalent sites and replacing its bound electron each time by a randomly polarized electron from the surroundings.

The extension of equation (20) to N muon states results in the following set of equations:

$$\dot{\vec{P}}_k(t) = \left(M_k - \sum_{l \neq k}^{N} \Lambda_{kl}\right) \cdot \vec{P}_k(t) + \sum_{l \neq k}^{N} \Lambda_{lk} \mathcal{A} \vec{P}_l(t) \tag{23}$$

with

$$\vec{P}^{\text{tot}}(t) = \sum_{k=1}^{N} \vec{P}_k(t) \tag{24}$$

The solution of this set of equations proceeds in a similar fashion to that for the individual Mu* state (equations (14, 15)), but aside from a few special cases, it cannot be performed analytically. The limit of complexity for such problems is set by the computer. The muon polarization is given by the sum

$$p_\mu^\alpha(t) = \sum_{k=0}^{N-1} \left[\sum_{l,\, \beta=1}^{15 \cdot N} U_{15 \cdot k + \alpha, l} U^{-1}_{l,\beta} P_\beta(0) \exp(D_u t) \right] \tag{25}$$

with $\alpha = 1, 2, 3$ denoting the x, y and z components of the muon polarization.

(c) *The transition from* Mu *to* Mu*

An example of the transformation model which can be solved analytically is the transition from an isotropic muonium state to an anisotropic muonium state with $\vec{n} \perp \vec{B}$ (Mu$\rightarrow$Mu*(90°)) in the absence of relaxation effects ($\nu_{\text{ex}} = 0$). Here we denote by $\Lambda = \Lambda_{12}$ the transition rate, by $\mathcal{H}$ the spin Hamiltonian for Mu (equation (1)) and by $\tilde{\mathcal{H}}$ the Hamiltonian for Mu* (equation (6)). We take E_n to be the energy eigenvalue of the eigenstate $|n\rangle$ of $\mathcal{H}$ ($\mathcal{H}|n\rangle = E_n|n\rangle$). The muon polarization then oscillates at frequencies ω_{mn} given by the energy differences:

$$\omega_{mn} = 2\pi\nu_{mn} = (E_m - E_n)/\hbar. \tag{26}$$

For Mu*(90°), the four transition frequencies observed in a transverse field experiment are given by

$$\begin{aligned}
\omega_{14} &= 2\pi\nu_{14} = \tfrac{1}{2}[\omega_0 - \tfrac{1}{2}\omega^* csc(2\psi) + (\omega_0 + \tfrac{1}{2}\omega^*) csc(2\chi)] \\
\omega_{12} &= 2\pi\nu_{12} = \tfrac{1}{2}[\omega_0 - \tfrac{1}{2}\omega^* csc(2\psi) - (\omega_0 + \tfrac{1}{2}\omega^*) csc(2\chi)] \\
\omega_{23} &= 2\pi\nu_{23} = \omega_{14} - \omega_0 \\
\omega_{34} &= 2\pi\nu_{34} = \omega_{12} - \omega_0
\end{aligned} \tag{27}$$

where the angles χ and ψ are defined by

$$\tan(2\psi) = \frac{-\frac{1}{2}\omega^*}{\omega_e - \omega_\mu}$$
$$\tan(2\chi) = \frac{\omega_0 + \frac{1}{2}\omega^*}{\omega_e + \omega_\mu} \tag{28}$$

The time-dependent, 15-component polarization $\vec{P}$ for such an irreversible process can be obtained from equations (18, 19) by setting $\Lambda_{21} = 0$. In the absence of relaxation effects, however, it is unnecessary to follow all 15 components, and the total muon polarization $\vec{p}_\mu^{\,\mathrm{tot}}(t)$ can be written in the following form:

$$\vec{p}_\mu^{\,\mathrm{tot}}(t) = \vec{p}_\mu(t)\exp(-\Lambda t) + \vec{p}_\mu^{\,\mathrm{tr}}(t) \tag{29}$$

where $\vec{p}_\mu(t)$ is the muon polarization in an undisturbed Mu state and where

$$\vec{p}_\mu^{\,\mathrm{tr}}(t) = \Lambda \int_0^t dt' \exp(-\Lambda t')\,\mathrm{Tr}\{\exp[-i\tilde{\mathcal{H}}(t-t')/\hbar]\rho(t')\exp[i\tilde{\mathcal{H}}(t-t')/\hbar]\cdot\vec{\sigma}\} \tag{30}$$

If the muon polarization is carried over from one state to the other but the electron polarization is lost, the density matrix at the time of the reaction t' is given by:

$$\rho(t') = \tfrac{1}{4}[1 + \vec{p}_\mu(t')\cdot\vec{\sigma}] \tag{31}$$

On the other hand, if the electron polarization is conserved during the transition, then $\rho(t')$ is given by:

$$\rho(t') = \exp(-i\mathcal{H}t'/\hbar)\rho(0)\exp(i\mathcal{H}t'/\hbar) \tag{32}$$

Integrating over all transition times t', one obtains

$$\begin{aligned}\vec{p}_\mu^{\,\mathrm{tot}}(t) = &\sum_{m,n,\tilde{m},\tilde{n}} [\langle m|\,\rho(0)\,|n\rangle\langle n|\,\vec{\sigma}\,|m\rangle - \vec{\mathcal{P}}_{\tilde{m},\tilde{n}/m,n}\exp(i\alpha_{mn}^{\tilde{m}\tilde{n}})] \\ &\times \exp[-(i\omega_{mn} + \Lambda)t] \\ &+ \sum_{m,n,\tilde{m},\tilde{n}} \vec{\mathcal{P}}_{\tilde{m},\tilde{n}/m,n}\exp(-i\tilde{\omega}_{\tilde{m}\tilde{n}}t + i\alpha_{mn}^{\tilde{m}\tilde{n}})\end{aligned} \tag{33}$$

where

$$\vec{\mathcal{P}}_{\tilde{m},\tilde{n}\,|\,m,n} = \langle\tilde{m}\,|\,m\rangle\langle m|\,\rho(0)\,|n\rangle\langle n\,|\,\tilde{n}\rangle\langle\tilde{n}|\,\vec{\sigma}\,|\tilde{m}\rangle\cos\alpha_{mn}^{\tilde{m}\tilde{n}} \tag{34}$$

and

$$\tan\alpha_{mn}^{\tilde{m}\tilde{n}} = \frac{\tilde{\omega}_{\tilde{m}\tilde{n}} - \omega_{mn}}{\Lambda}. \tag{35}$$

Two points should be noted: (i) the damping rate of the precursor Mu precession signals (at frequencies ω_{mn}) is simply the transition rate Λ. (ii) The amplitudes of the final state Mu* signals ($\tilde{\omega}_{\tilde{m}\tilde{n}}$) are determined by the angle α and show a maximum for $\alpha = 0$ (i.e. for $\tilde{\omega}_{\tilde{m}\tilde{n}} = \omega_{mn}$).

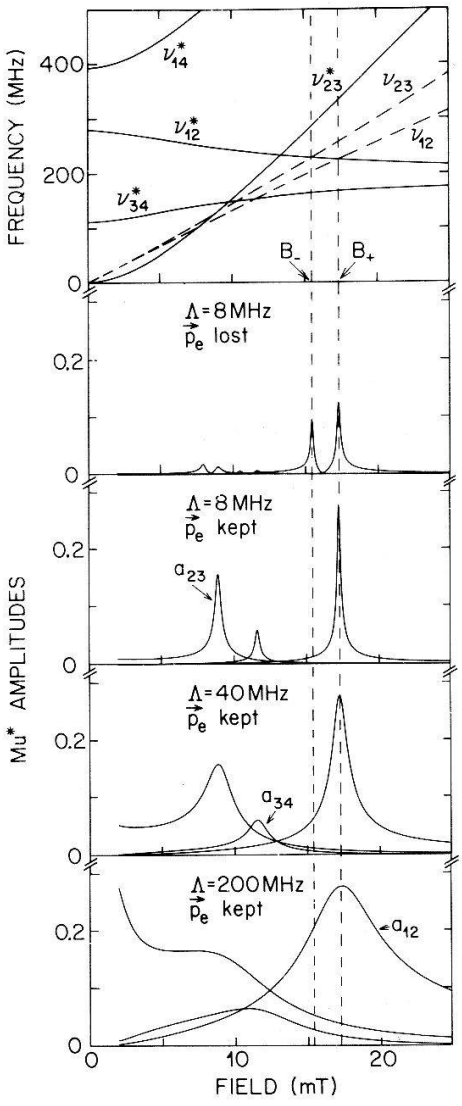

Figure 3
Upper section: expected Mu* and Mu precession frequencies for the magnetic field along the $\langle 110 \rangle$ axis in diamond, which coincide at particular fields B_- and B_+. Lower sections: the theoretically predicted Mu* amplitudes resulting from a Mu$\rightarrow$Mu*(90°) with $A_s(\text{Mu}^*)/A(\text{Mu}) > 0$ for various transition rates Λ under the assumption of the loss ($\vec{p}_e$ lost) and conservation ($\vec{p}_e$ kept) of the electron polarization.

We can now apply this description to the experimentally investigated case of a Mu$\rightarrow$Mu*(90°) transition in diamond [2, 13] with conservation of the electron polarization. With the Mu and Mu* *hf* parameters determined for diamond, the Mu* frequency 1–2 as function of the applied field crosses the triplet muonium frequencies at the field values $B_- = 15.4\,\text{mT}$ and $B_+ = 17.2\,\text{mT}$ (see equation (27) and Fig. 3). If the Mu *hf* interaction is taken to be positive (by analogy with vacuum Mu), then a resonantly large fraction of the muon polarization will be carried over from Mu to Mu* at either B_- or B_+, depending upon whether $A_s(\text{Mu}^*)/A(\text{Mu})$ is less than or greater than zero. The Mu* 3–4 signal precesses in the opposite sense and thus does not show a resonance.

The existence of a *single* resonant field follows from the assumption that the electron polarization is *conserved* during the transition. Due to the smallness of the Mu* *hf* coupling constants, the Mu* electron spin is decoupled from the muon spin at magnetic fields greater than ~10 mT. For a positive A_s, the Mu* 1–2 signal then corresponds to a muon spin flip with the electron spin up, and for a negative A_s to the electron spin down. Furthermore, the Mu hyperfine states $|1\rangle$

and $|3\rangle$ are also eigenstates of the electron spin S_z with the electron spin up and down, respectively. The factors $\langle \tilde{m} \mid m \rangle$ and $\langle n \mid \tilde{n} \rangle$ in equation (34) thus imply that a coincidence between $\tilde{\omega}_{12}$ and ω_{12} ($\tilde{\omega}_{12}$ and ω_{23}) will cause a resonant polarization transfer for A_s positive (negative). In the *absence* of electron spin conservation, this selection does *not* occur, and an enhanced transfer of muon polarization is expected at *both* B_- and B_+.

(d) *Transitions between two similar* Mu *states*

High-field experiments on the cuprous halides [15] show transitions between Mu^{I} and Mu^{II}, two isotropic states with almost equal *hf* constants. To apply our transformation model to this case, we begin by writing the precession frequencies for an undisturbed Mu state as

$$\begin{aligned}
\omega_1 &= 2\pi\nu_1 = \tfrac{1}{2}[\omega_0 + \omega_e - \omega_\mu - \omega_0 csc(2\chi)] \\
\omega_2 &= 2\pi\nu_2 = \omega_1 - \omega_0 \\
\omega_3 &= 2\pi\nu_3 = \tfrac{1}{2}[\omega_0 + \omega_e - \omega_\mu + \omega_0 csc(2\chi)] \\
\omega_4 &= 2\pi\nu_4 = \omega_3 - \omega_0
\end{aligned} \tag{36}$$

with

$$\tan(2\chi) = \frac{\omega_0}{\omega_e + \omega_\mu} \tag{37}$$

We write the *hf* constants of the two states as

$$\omega_0^{I/II} = \omega_0 \pm \Delta\omega_0 \tag{38}$$

We assume that the following conditions hold: (i) the *hf* constants are similar ($\Delta\omega_0 \ll \omega_0$), (ii) we are dealing with the transverse subsystem ($\vec{p}_\mu(0) \perp \vec{B}$), (iii) the electron polarization is conserved in the transition and (iv) there is no electron exchange ($\nu_{ex} = 0$). Under these circumstances, the transition model yields analytical solutions. We expect in general 8 precession lines

$$\lambda_n^{\pm} \cong \tfrac{1}{2}\{i(\omega_n^{I} + \omega_n^{II}) - (\Lambda_{12} + \Lambda_{21}) \pm \sqrt{[i(\omega_n^{I} - \omega_n^{II}) - (\Lambda_{12} - \Lambda_{21})]^2 + 4\Lambda_{12}\Lambda_{21}}\} \tag{39}$$

where $n = 1, \ldots, 4$. ω_n^i with $i = I$, II are the oscillation frequencies for the undisturbed Mu states with the *hf* constants given by equation (38). Note that the real part of $-\lambda_n^{\pm}$ represents a relaxation rate, while the imaginary part is an oscillation frequency. The time-dependent muon polarization is given by:

$$\begin{aligned}
p_\mu(t) = \tfrac{1}{2} \sum_{n=1}^{4} \Bigg\{ & W_n \frac{\Lambda_{12} + a_n}{\Lambda_{12}\Lambda_{21} + a_n^2} [a_n p_\mu^{I}(0) + \Lambda_{21} p_\mu^{II}(0)] \exp(\lambda_n^{+} t) \\
& + W_n \frac{\Lambda_{21} - a_n}{\Lambda_{12}\Lambda_{21} + a_n^2} [\Lambda_{12} p_\mu^{I}(0) - a_n p_\mu^{II}(0)] \exp(\lambda_n^{-} t) \Bigg\}
\end{aligned} \tag{40}$$

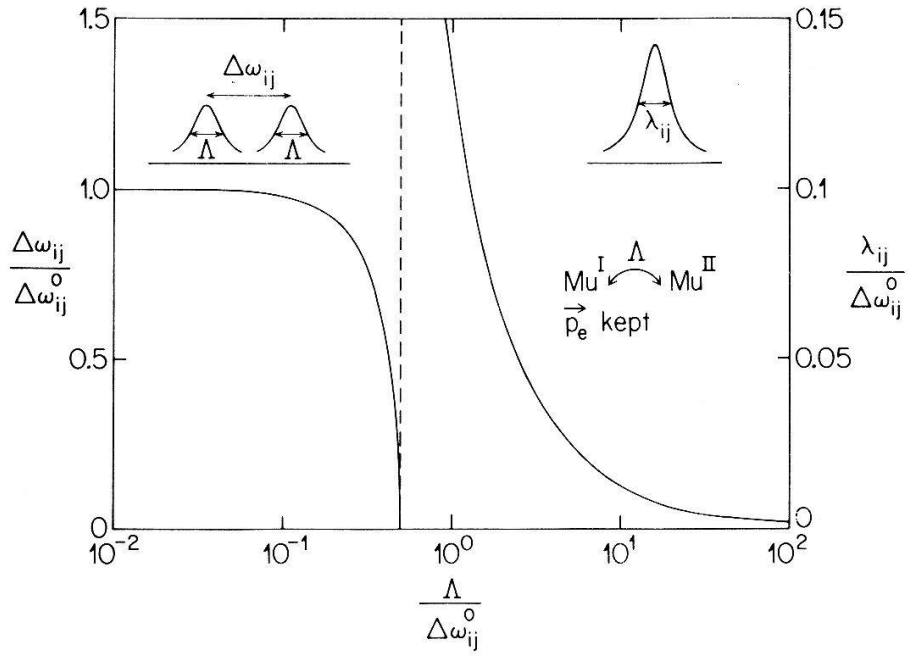

Figure 4
'Universal' plot of the rate-dependent line separation $\Delta\omega_n$ and linewidth λ_n for Mu hopping between sites with different but similar *hf* frequencies. The quantities are normalized to the linewidth separation without jumps $\Delta\omega_n^0$ and plotted against the normalized jump rate $\Lambda/\Delta\omega_n^0$.

where

$$a_n = \lambda_n^+ - (i\omega_n^{II} - \Lambda_{21})$$
$$W_n = (\cos^2\chi, \cos^2\chi, \sin^2\chi, \sin^2\chi) \tag{41}$$

$p_\mu^I(0)$ and $p_\mu^{II}(0)$ denote the initial muon polarizations in states I and II, respectively. Note that in the high field limit only contributions with $n = 1, 2$ are expected. The irreversible case $Mu^I \rightarrow Mu^{II}$ is obtained by setting $\Lambda_{21} = 0$; we then obtain a relaxed precursor state and an undamped final state.

When both transition rates are equal ($=\Lambda$), the discriminant in equation (39) is real and, depending on its sign, a splitting occurs in the relaxation rates (if positive) or in the oscillation frequencies (if negative). In the first case (small Λ), two distinct muon states are visible. A plot of the frequency splitting $\Delta\omega_n$, normalized to the difference $\Delta\omega_n^0 = \omega_n^I - \omega_n^{II}$ for $\Lambda = 0$, is plotted in Fig. 4. For rates Λ larger than $\Delta\omega_n^0/2$, the frequency splitting vanishes, and a single line ω_n is seen corresponding to a Mu state with the *hf* constant equal to the averaged value ω_0. Each frequency now appears twice, with different relaxation rates. With increasing Λ, one of the damping rates decreases (see Fig. 4), while the other approaches asymptotically 2Λ.

III. Experimental details

(a) *The μSR-technique*

The high-intensity accelerators, the so-called meson factories, make it possible to use positive muons as unique microscopic probes in solid-state physics.

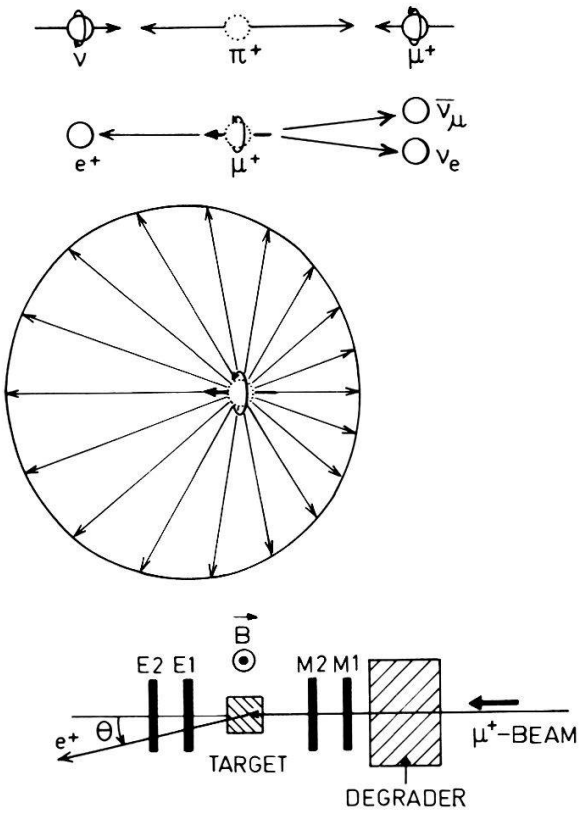

Figure 5
Upper part: the π^+ and μ^+ decay. Center part: the angular distribution of the decay positrons with respect to the μ^+ spin. Lower part: a simplified diagram of the counter arrangements in a μSR experiment. The scintillation counters M1 and M2 register the incoming muons and E1 and E2 the decay positrons.

The muon is a spin-$\frac{1}{2}$ particle and belongs to the family of leptons. Its mass is 207 times the electron mass or $\frac{1}{9}$ of the proton mass. A feature of the muon which is vital to its use in solid state experiments is its parity-violating decay (with a mean lifetime of 2.2 μs) into a positron and two neutrinos with the positron emitted *preferentially along the muon spin direction* (see Fig. 5). This fact makes it possible to monitor the time evolution of the muon polarization.

In a muon-spin-rotation (μSR) experiment [3, 24], polarized positive muons are stopped in the material to be investigated, and the decay positrons are recorded as a function of the time after a muon stop. In the short time of thermalization ($\sim 10^{-12}$ s) the muon maintains its polarization. When a magnetic field $\vec{B}$ is applied perpendicular to the initial muon polarization, a free muon precesses with the Larmor frequency ω_μ (see equation (5)). Due to the anisotropic muon decay, the exponential muon decay, as monitored in a particular direction in the plane of precession, is modulated at the frequency ω_μ. If muonium ($\mu^+e^- = \mathrm{Mu}$) is formed in a solid, precession components are observed at frequencies which correspond to transitions between the hyperfine levels of the spin Hamiltonian given in equations (1, 3). The upper limit for the rate at which data can be collected in a μSR experiment is given by the requirement that no more than one muon be present in the sample at given time, since the parent muon of a decay positron must be uniquely identified.

(b) *Experimental setups*

All the present measurements were performed at the Swiss Institute for Nuclear Research (SIN). Two different μSR spectrometers were used, depending on the type of experiment and on sample size.

For measurements on thin (down to 30 mg/cm^2) samples a μSR spectrometer specially designed for surface muons ($p_\mu = 29$ MeV/c from pion decay at rest) was used. Surface muons are 100% backward polarized, and their range is approximately 150 mg/cm^2. Therefore thin windows of $\simeq 130\,\mu$m made from Kapton and $\simeq 20\,\mu m$ Cu–Be alloy were used for the cryostat and the oven, respectively. The typical sample area was 0.5 cm^2. Rotatable Helmholtz coils could produce magnetic fields up to 0.4 T, and the earth's field was compensated by three pairs of 'zero-field' coils to better than 2 μT. A He gas-flow cryostat and a hot-finger oven enabled measurements in the temperature range 6–800 K. Below 300 K, the sample temperature was measured with platinum and carbon resistors. In the oven the temperature was measured with a Ni–NiCr thermocouple. Two independent sets of positron counters allowed either large-acceptance forward–backward counting for zero field and longitudinal field experiments or up–down counting for transverse field experiments. By replacing the thin incident muon counter with a thicker one, this μSR apparatus could be used as well with conventional muons ($p_\mu > 50$ MeV/c).

For experiments which require a high time-resolution and a large applied magnetic field, a dedicated μSR spectrometer was developed [15] (see Fig. 6). The object of the high magnetic field was to quench the nuclear hyperfine interaction of muonium [25] to produce narrow precession lines, thus allowing measurements of muonium in non-metals with a high concentration of nuclear moments. The resulting Mu precession frequencies lie in the GHz region. During

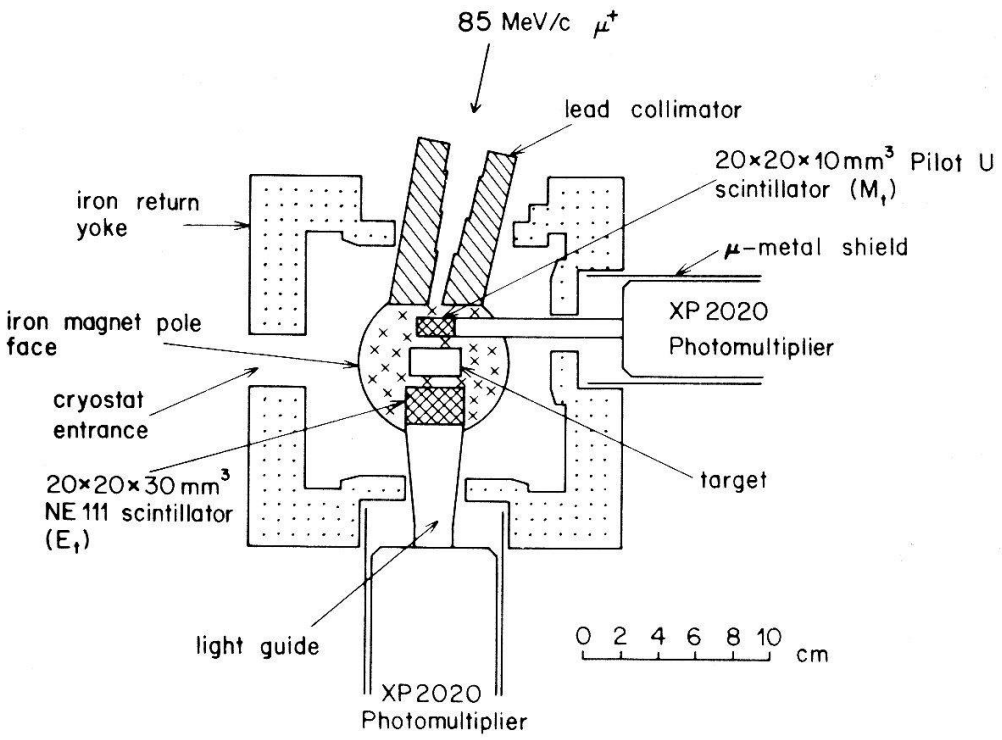

Figure 6
Schematic diagram of the high timing resolution (220 ps FWHM) apparatus used to resolve precession frequencies in a large (1.2 T) transverse magnetic field. The return yoke of the compact iron-core electromagnet reduces the magnetic stray field and thus permits the use of short light guides between the fast plastic scintillators and photomultipliers.

the experiments on the copper halides, muons polarized in the forward direction were used with a momentum of 85 Mev/c. Due to kinematic depolarization, the experimentally-determined muon polarization was reduced to approximately 80%. The range width for this momentum is approximately 2 g/cm^2. A compact iron-core electromagnet with return yoke allowed measurements in transverse fields from 0.01 up to 1.2 T. The stray field of the magnet was less than 10 μT 10 cm from the magnet center. This allowed the use of short light guides from the scintillation counters to the field sensitive photomultipliers – a requirement for achieving a high time-resolution. With fast scintillators, quartz light guides, selected XP-2020 photomultiplier tubes and bases, special coaxial signal cables, constant fraction discriminators and temperature-regulated electronics, this apparatus achieves a time resolution of 220 ps (FWHM) [15]. This allowed measurements of frequencies up to approximately 2.3 GHz. The sample, with a typical size of $14 \times 16 \times 24$ mm^3 was cooled and heated in a He gas flow cryostat and hot finger oven, respectively.

(c) *Electronics and data-acquisition*

A diagram of the electronics used for the high-field, high-timing resolution apparatus is shown in Fig. 7. The anode pulses from the detectors are discriminated by Ortec 583 constant fraction differential discriminators and, if in coincidence with the appropriate logic signals, are fed into the start and the stop inputs of a time-to-amplitude converter (TAC). A logic box and pile-up gate were

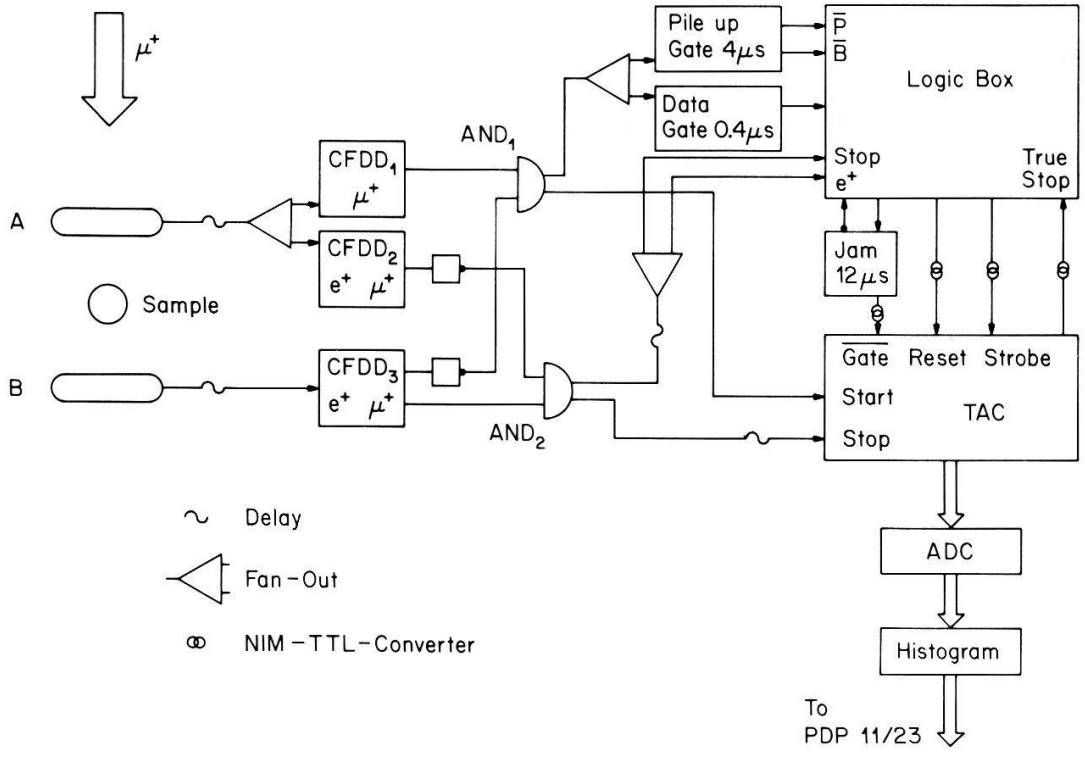

Figure 7
Electronic setup used for the high-field, high-timing resolution apparatus shown in Fig. 6.

used to reject events resulting from two detected positrons or two stopped muons during one measuring cycle. The TAC was coupled to a 8000-channel analog-to-digital (ADC) converter (LeCroy model 3512). A TAC setting of 45 ps/channel was necessary to resolve the high Mu frequencies, and this limited the length of the time spectra to 400 ns. Calibration of the TAC was performed with a 100 MHz quartz time calibrator that produced lines in the time spectrum with a well-defined separation of 10 ns ± 10 ppm. The direct coupling of the ADC to a histogramming memory (HM) module (LeCroy model 3588) permitted data taking at a high rate with the computer free for other tasks.

If no high frequencies were expected (<500 MHz), a LeCroy model 4202 time-to-digital (TDC) converter based on a quartz clock, and again directly coupled to the HM, was used instead of the TAC and ADC. The 8 k spectrum could be divided into several subspectra (e.g. forward, backward).

A data acquisition system was developed based on an LSI-11/23 computer coupled to a CAMAC crate. The memory size of the LSI was 256 KB, and a 10 MB winchester drive was installed. The subroutines to drive the CAMAC controller were written in Assembler, while Fortran was used for the rest of the program. A Fast-Fourier Transformation allowed an on-line analysis of the data. Using a video display driver, a second television screen could display the time spectrum updated by the LSI from the HM every few seconds. A ROAD C interface in CAMAC permitted automated setting of the applied magnetic field at the sample.

(d) *Data analysis*

The general form of a μSR spectrum consists of an exponential decay, modulated by a sum of damped sinusoidal oscillations corresponding to the time-dependent muon polarization:

$$N(t) = N_0 e^{-t/\tau_\mu}[1 + X(t)] + B \tag{42a}$$

$$X(t) = \sum_{j=1}^{n} a_j R_j(t) \cos(2\pi\nu_j t + \Phi_j) \tag{42b}$$

N_0 is a normalization constant, τ_μ is the muon lifetime (2.2 μs for positive muons) and B is a time-independent background. The parameters a_j, ν_j, and Φ_j are the amplitudes, precession frequencies, and initial phase angles of the n different contributions to the muon polarization. The relaxation functions $R_j(t)$ are assumed to be exponential

$$R_j(t) = \exp(-\lambda_j t) \tag{43}$$

or Gaussian

$$R_j(t) = \exp(-\sigma_j^2 t^2) \tag{44}$$

To determine the number n of significant signals and their approximate frequencies, the modulation spectra $X(t)$ were Fourier-transformed. Least-square

fits of the time spectra to equation (42a) were then performed. It was often found to be advantageous, particularly if there were a large number of weak signals, to perform least-square fits of the Fourier transform of equation (42b) to the complex *Fourier* spectra. A comparison showed that the two methods yielded identical results.

For high frequencies, the effects of the finite time resolution [5] of the particle detection system must be considered. If one assumes a Gaussian resolution function with a FWHM of Δt, then the observed amplitude a_{obs} of a signal at frequency ν is given by:

$$a_{\text{obs}} = a_{\text{theo}} \exp\left[-\frac{(\pi \nu \, \Delta t)^2}{4 \ln 2} \right] \tag{45}$$

where a_{theo} is the expected amplitude. The time resolution Δt could be calibrated using observations of the two high field Mu precession frequencies.

To obtain absolute amplitude values, the measured precession amplitudes, after correction for finite time resolution, were normalized to the maximum experimental amplitude, taken from the free-muon precession in a metal such as copper.

(e) *Sample specific details*

1. *Diamond.* The diamond experiments were performed using 28 MeV/c muons on a single crystal sample with no evidence of nitrogen impurities in its infrared absorption spectrum. The diamond was in a high-vacuum hot finger oven with the applied magnetic field along $\langle 110 \rangle$. Fine orientation adjustments of the crystal were made based on the Mu* line splitting. In this orientation, two $\langle 111 \rangle$ symmetry axes were at $\theta = 90°$, and the other two at $\theta = 35.26°$ with respect to the external field. The measurements were performed in the temperature region 300–600 K, and magnetic fields up to 25 mT were applied. The uncertainty of the sample temperature was less than 0.1 K, and that of the field was less than 0.4%. To minimize background, muon decay positrons were detected perpendicular to the incoming beam. Our time resolution of approximately 900 ps FWHM allowed the observation of frequencies up to 500 MHz. In each run, $2 - 5 \times 10^6$ good muon decay events were accumulated in each of two time histograms, of which approximately 20% were from muons which stopped in the copper target holder. The precession frequencies, their amplitudes and their relaxation rates were extracted by multi-frequency fits to the μSR time histograms. The transition model (equations (33–35)) was fitted to the weighted average of the amplitudes from both histograms. In the analysis, account was taken of the temperature dependence of the Mu* hyperfine constants [2].

2. *Cuprous halides.* All measurements on the cuprous halides were performed in the high-field (1.2 T), high-timing resolution apparatus using 85 Mev/c muons. Below room temperature, single crystals of CuCl, CuBr and CuI were investigated, which had been cut from rods grown from the melt by C. Schwab using a traveling-heater technique [26]. The dimension of the crystals was

approximately 12 mm in diameter by 12 mm long. The crystals were oriented ($\langle 111 \rangle \parallel \vec{B}$) in the case of CuCl and CuBr, but not in the case of CuI, and cooled in a He-float cryostat. The measurements above room-temperature were performed in a hot finger oven on a polycrystalline CuCl sample in a glass ampoule of approximately 8 mm in diameter and 12 mm length. Up to 445 K, high-frequency Mu signals were observed, and therefore the high-resolution setting of 45 ps/channel was used on the TAC. Above 445 K, only the slow μ^+ precession was observed, and the setting was changed to 200 ps/channel. For the muonium runs, up to 15×10^6 good muon decay events were accumulated, and for the μ^+ runs typically 2.5×10^6. Approximately 90% of the incoming muons stopped in the crystals, but this fraction was reduced to 75% for the polycrystalline sample due to its smaller size. Correction for this difference was made by assuming equal muonium formation probabilities in the two samples. The timing resolution Δt, obtained from measurements on a crystalline quartz sample at room temperature, was 205(13) ps and 271(15) ps for the low-temperature and high-temperature experiments, respectively.

3. *High-purity silicon.* For these measurements, surface muons (28 MeV/c) were used which were spin-rotated upstream of the experiment with a Wien-filter by an angle of 65° relative to the muon momentum. A single counter perpendicular to the incoming beam detected the decay positrons. In this way, background due to beam contaminants was reduced to a minimum, and bending of the muon beam was avoided, since the applied field was parallel to the incoming beam.

The silicon sample used was a float-zone single crystal with a resistivity of 13500 Ω-cm and a specified concentration of electrically active impurities of $\sim 10^{12}$ cm^{-3} (p-type). The crystal was oriented with the $\langle 110 \rangle$ axis perpendicular to the applied field. Measurements were performed in the temperature region 40–700 K in applied fields of 10.6 and 287.1 mT. Depending on the temperature region, a He-flow cryostat or a hot finger oven was used. The uncertainty of the sample temperature was less than 0.2 K, and that of the external field was 45 μT. During the temperature scan at 10.6 mT, 2×10^6 good muon decay events were accumulated for each run in a single histogram with 7400 usable channels, each 625 ps wide. The rate of accumulated events was 800 s^{-1} at a muon stop rate of 6200 s^{-1}. The timing resolution was obtained from measurements on crystalline quartz SiO_2 at various fields and found to be $\Delta t = 1.44(4)$ ns. The precession amplitudes were corrected for finite timing resolution and normalized to the maximum experimental asymmetry taken to be the free-muon precession amplitude in brass.

IV. The Mu and Mu* states in diamond

(a) *Sign determination of the* Mu* *hyperfine parameters*

The first evidence for a Mu to Mu* transition in diamond came from zero-field powder measurements [2]. Three Mu* μSR signals are expected in

zero-field. By measuring the temperature dependence of the Mu* signal strength, Holzschuh et al. [2] observed increases in the three amplitudes which occur at different temperatures. The explanation was found to be a Mu→Mu* transition with the electron spin conserved during the transition. Meier [11] treated the zero-field case, and predicted as well that a determination of the sign of the Mu* hyperfine parameters would be possible in experiments with a single crystal oriented in an external magnetic field.

With the electron polarization conserved during the transition, a field scan at constant temperature should yield a 1–2 Mu* precession amplitude with a resonant maximum at either B_- or B_+, depending on the sign of A_s (see Section II.(c)). The width of this resonance is a function of the transition rate and therefore temperature-dependent; a definitive sign determination requires a narrow resonance and hence a measurement at as low a temperature as possible.

A first experiment [13] on a nitrogen-rich crystal showed the predicted resonance, but a sign determination was not possible due to relaxation broadening. It is believed that Mu trapping at the nitrogen impurities was the source of this broadening. In the present measurements, a nitrogen *poor* diamond (type IIb) was used, resulting in narrow precession lines and a sharp resonance.

Field scans were performed at 454 and 494 K, and the field was applied parallel to $\langle 100 \rangle$ and was varied from 7.8 mT to 25.7 mT in the vicinity of the frequency crossing. Note that with the applied magnetic field along $\langle 110 \rangle$, there are two Mu* centers with $\vec{n} \perp \vec{B}$ (Mu*(90°)) and therefore the same precession frequencies. Combined fits of the transition model equations (33–35) to the amplitudes of both Mu* lines $\nu_{12}(90°)$ and $\nu_{34}(90°)$ were made under the assumptions that a temperature-independent 'prompt' Mu* fraction f_1 is always present and that a Mu fraction f_2 is a precursor for Mu*. Such a 'prompt' Mu* fraction can be explained by almost instantaneous Mu* formation for a particular fraction of the incoming muons. This leads to total four contributions which must be added in phase.

The amplitude of the 1–2 Mu* line showed a single resonance at B_- (see Fig. 8), establishing that the electron polarization is conserved during the transition (see Fig. 3) and that the isotropic part A_s of the Mu* hyperfine interaction is *negative*. It is known from μSR experiments that A_s and A_p have the opposite sign in diamond [2]. For comparison, the dot-dashed curve in Fig. 8 shows the expected results for a positive A_s and negative A_p and unchanged values for the other fit parameters. The fitted transformation rate Λ was found to be $46(5) \times 10^6\,s^{-1}$ at 454 K and $142(12) \times 10^6\,s^{-1}$ at 494 K.

(b) *Temperature dependence of the* Mu *to* Mu* *transition rate*

As mentioned in Section II.(c), in the absence of additional depolarization such as from trapping at impurities, the damping rate of the precursor Mu state is equal to the Mu→Mu* transition rate Λ. The temperature dependence of the Mu relaxation rate was studied in the range 300 K to 400 K in an applied field of 1.25 mT. At this low field, the Mu precession frequencies ν_{12} and ν_{23} are centered

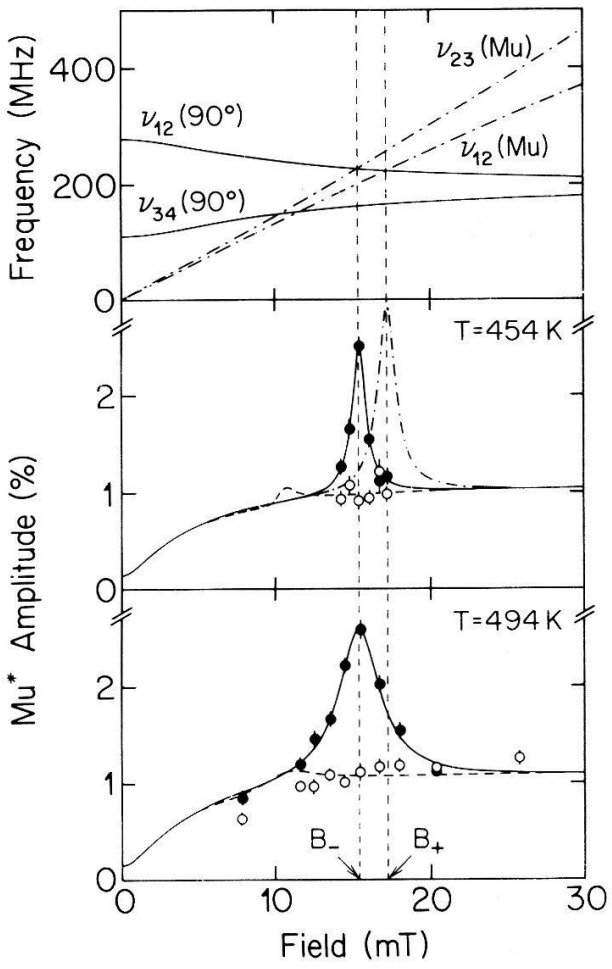

Figure 8
Expected Mu and Mu* precession frequencies for the magnetic field along the ⟨110⟩ axis in diamond. Also shown are the measured and fitted amplitudes of the Mu* precession signals 1–2 (solid circles, solid curves) and 3–4 (open circles, dashed curves) as a function of the applied field at 454 K and 494 K. The resonant maximum at the field $B_- = 15.4$ mT establishes that $A_s(\mathrm{Mu}^*)/A(\mathrm{Mu}) < 0$. For comparison, the dot-dashed curve shows the expected resonance at B_+ for the opposite sign (>0).

at 17.1 MHz with an unresolved splitting of ~0.18 MHz. With account taken of the splitting, a fit of the Mu relaxation rate λ to the Arrhenius law

$$\lambda(T) = \Lambda(T) + \lambda_0 = \Psi \exp(-U/kT) + \lambda_0 \tag{46}$$

yielded the dot-dashed curve in Fig. 9. λ_0 denotes a temperature-independent background.

At still higher temperatures, the transition rate Λ can be determined from the temperature-dependent increase of the Mu* amplitude (see Fig. 10). Such measurements were performed from 300 K to 660 K in an applied field of 16.5 mT, i.e. between the crossover fields B_- and B_+. At 373 K, strongly damped Mu signals are still visible. The measured Mu*(90°) precession amplitudes as function of temperature are presented in Fig. 9. The constant value for $T < 400$ K corresponds to the prompt Mu* fraction f_1. The shift of the rise in the 3–4 amplitude to higher temperatures is a consequence of its opposite sense of precession (see equation (27)). A second increase of the Mu* amplitudes, from the transfer of the Mu precession components 1–4 and 2–3, at frequencies higher than 3 GHz, is expected above 670 K. The solid and dashed curves in Fig. 9 are the results of a fit to the transition model (equations (33–35)) assuming an Arrhenius law for the transition rate Λ.

Values of $\Lambda(T)$ are thus available from three different sources: i) from the

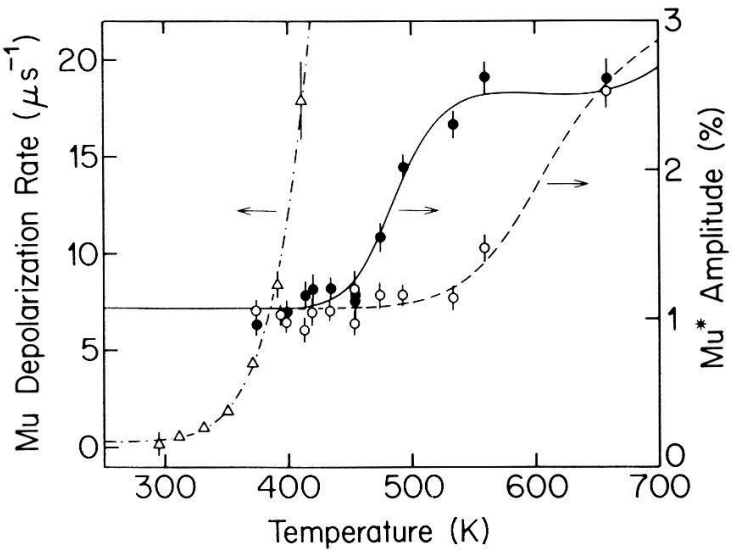

Figure 9
Mu damping rate of diamond for a field of 1.25 mT (triangles and left-hand scale) as a function of sample temperature. The dot-dashed curve is a fit to an Arrhenius law. Also shown are the measured amplitudes of the 1–2 (solid circles) and 3–4 (open circles) precession signals for Mu*(90°) centers in a field of 16.5 mT (right-hand scale). The solid and dashed curves are fits to the Mu to Mu* transition model assuming an Arrhenius law for the transition rate.

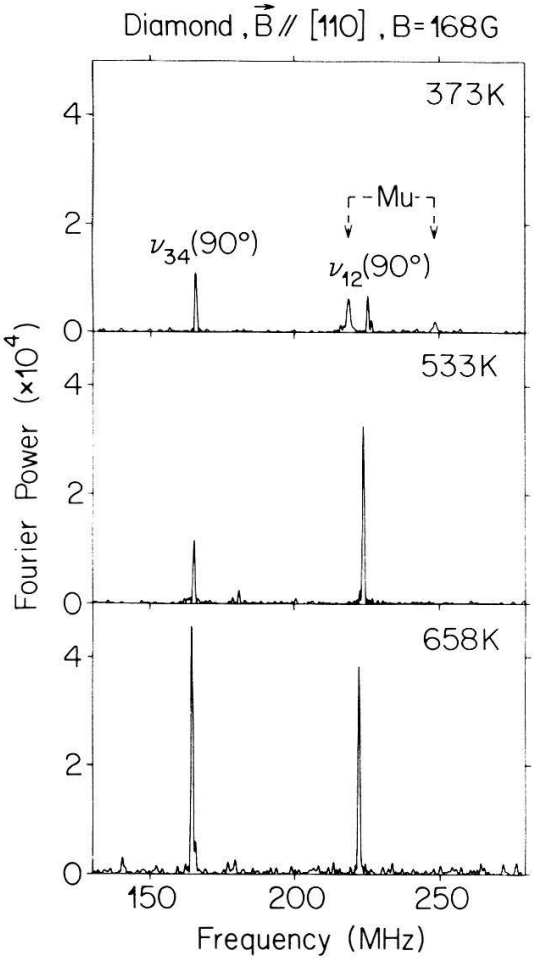

Figure 10
The μSR frequency spectra in a type-IIb diamond with $\vec{B} \parallel \langle 110 \rangle$ in a transverse magnetic field of 16.8 mT for different temperatures. The shift of the rise in the Mu* 3–4 signal strength to higher temperatures is a consequence of its opposite sense of precession. Note that rapidly damped Mu lines are still observed at 373 K.

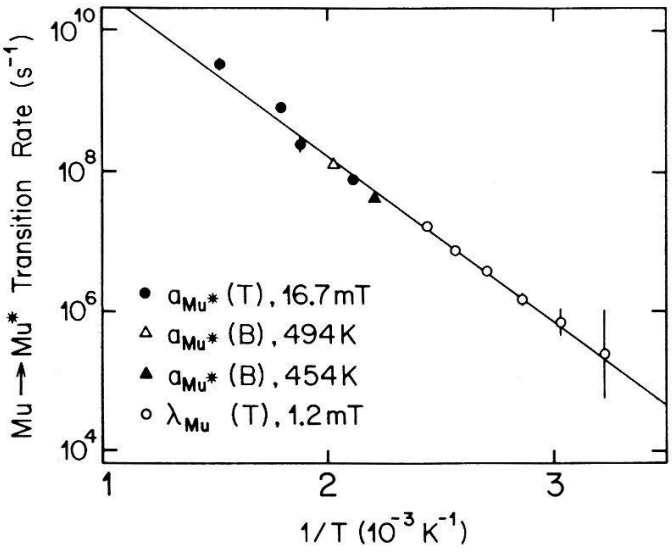

Figure 11
Experimental values of the temperature-dependent Mu→Mu* transition rate Λ obtained from various experiments as explained in the text. The solid line is a fit to an Arrhenius law.

field-dependent Mu* amplitude at 454 K and 494 K ii) from the temperature-dependent Mu relaxation rate (minus the temperature-independent term λ_0) iii) from the temperature-dependent Mu* amplitudes. A global fit to these values was performed to an Arrhenius law with the resulting values

$$\begin{aligned} \Psi &= 1.14(28) \cdot 10^{13}\,\mathrm{s}^{-1} \\ U &= 0.476(9)\,\mathrm{eV} \end{aligned} \tag{47}$$

and the results are shown in Fig. 11. Note that a single Arrhenius law describes the available data over more than 5 orders of magnitude in Λ.

The entire muon polarization in the type-IIb diamond at room temperature could be accounted for by the prompt Mu* fraction $f_1 = 25(2)\%$ and the precursor Mu fraction $f_2 = 75(6)\%$. Any missing fraction was less than 6%. The temperature-independent quotient f_1/f_2 obtained as a weighted average from all the measurements was 0.328(12).

(c) *Temperature dependence of the* Mu *hyperfine parameter*

The temperature dependences of the Mu hyperfine parameter A in Si and Ge have been accurately measured with the zero-field, high time-resolution technique [5]. No measurement of $A(T)$ for Mu in diamond has yet been reported. In our type-IIb sample, Mu precession was observed at the frequencies ν_{12} and ν_{23} up to 410 K (see Fig. 9) in fields up to 45.3 mT. Together with the precession frequency $\nu_\mu = 135.54\,\mathrm{MHz/T} \times B$ of the free muon, these measurements yield the Mu hyperfine frequency A according to

$$A = 2\left[\frac{\nu_{12}\nu_{23} + \nu_\mu(\nu_{12} + \nu_{23} + \nu_\mu)}{\nu_{23} - \nu_{12}}\right]. \tag{48}$$

Table 3
The hyperfine coupling constant A and electronic g-factor g_e for isotropic Mu in diamond as a function of temperature.

T (K)	A (MHz)	g_e
6[a]	3711(21)	−2.0034(17)
293.0	3710.9(1.0)	−1.9971(56)
373.5	3693.0(8.6)	−1.9972(57)
398.5	3568(69)	−2.005(12)

[a]) Taken from Ref. 2.

In addition, the electronic g-factor g_e can be obtained from the relation:

$$g_e = -g_\mu \frac{m_e}{m_\mu}\left[\frac{\nu_{12}+\nu_{23}}{\nu_\mu}+1\right]. \tag{49}$$

The experimental values for A and g_e are summarized in Table 3. Because of the limited data available, it is not possible to discriminate between the Debye and the Einstein model for $A(T)$ discussed in Refs. 2 and 27.

(d) *Discussion*

Our study of the Mu→Mu* transition in diamond clearly establishes that the isotropic part of the Mu* hyperfine interaction is *negative*. This implies that Mu* is not simply a distorted version of isotropic Mu, since this would imply a positive electron spin density at the muon. A more promising model of Mu* is a paramagnetic complex similar to a molecular radical with the unpaired electron removed from the muon. The weak negative spin density at the muon is then the result of an 'exchange polarization' mechanism. The Mu* hyperfine constants A_s and A_p have been studied previously in diamond, silicon and germanium as a function of temperature [28]. Although in that work the incorrect sign for A_s was assumed, in view of the similar behavior for the three materials, it was convincingly argued that the same sign assignments for A_s and A_p should apply. A further result of the present investigation is that the thermally-activated transition from Mu to Mu* in diamond proceeds without loss of the electron polarization.

At room temperature, Mu and Mu* are observed simultaneously in the μSR spectra; both are formed promptly upon muon implantation. The thermally-activated conversion of Mu to Mu*, together with the fact that Mu* is observable [2] in diamond up to at least 1100 K establishes that Mu* is the more stable state. In Si and Ge, Mu* disappears above 165 and 85 K, respectively, perhaps under the influence of free carriers [29, 30].

While normal muonium is generally accepted to be at a tetrahedral interstitial site in the diamond lattice [31–38], the site of Mu* is still uncertain. The anisotropic *hf* interaction of Mu* implies that it is immobile. Of the many models that have been suggested for Mu*, the two which are being most seriously developed are (i) muonium which occupies a host-ion vacancy [39–43] and (ii)

muonium situated near the center of a host bond [44–48]. Both of these models appear consistent with $A_s < 0$, but the high Arrhenius prefactor $\Psi \simeq 10^{13}\,s^{-1}$ for the Mu→Mu* transition rate $\Lambda(T)$ is incompatible with a model where the precursor Mu searches for a preexisting lattice vacancy in order to become Mu*. This value for Ψ is comparable to an optical phonon frequency in diamond and hence is approximately the maximum possible jump rate for Mu, implying that only a *single jump* is required by Mu to form Mu*. A cluster calculation [46, 48] of the potential energy surface traversed by muonium from the tetrahedral interstitial site to the center of a strongly stretched C–C bond in diamond reproduces our observation that the Mu state is metastable, but it apparently overestimates the true barrier height. Further support of the bond-centered model for Mu* has been provided by the observation of its resolved nuclear hyperfine structure in Si [49], and with a single Ga and a single As in GaAs [50].

V. The $Mu^I \rightarrow Mu^{II} \rightarrow \mu^+$ transition in CuCl

(a) *The muonium hyperfine parameters for* Mu^I *and* Mu^{II}

The muon-spin rotation frequency spectra for CuCl, CuBr and CuI in a transverse magnetic field of 1.2 T are shown in Fig. 12. The two pairs of lines ν_i^I and ν_i^{II} (see equation (36)) observed in CuBr and CuCl at low temperatures are attributed to different muonium centers Mu^I and Mu^{II}. In CuI only a single pair of lines is observed. The frequencies are independent of crystal orientation, indicating that the hyperfine interaction for these centers is isotropic. The *hf* coupling constant $A = \omega_0/2\pi$ is thus simply given by $\nu_1^i + \nu_2^i$, for $i = I, II$ (see equation (36)). The temperature dependence of the *hf* parameters for all three samples is shown in Fig. 13. Except for the Mu^{II} center in CuBr, the last data point plotted corresponds to the highest temperature at which the state can be seen (see Table 2). At higher temperatures, the signals were rapidly damped.

In CuI only one muonium center is observed with decreasing *hf* parameter as a function of temperature. In CuCl and CuBr the muonium center with the larger *hf* coupling constant (Mu^I) is only observed at low temperatures.

The temperature-dependence of the *hf* parameters for CuBr and CuCl are very similar. In contrast to Mu in other semiconductors, their *hf* parameters generally *increase* with increasing temperature. At low temperatures, a Debye model [2, 15] was fitted to the measured *hf* parameters in the Cu halides. Such a model assumes that the temperature variation in the *hf* parameter is due to muonium interaction with a Debye spectrum of acoustic phonons, and predicts an $A(T)$ of the form:

$$A(T) = A(0)\left[1 - \kappa\left(\frac{T}{\Theta_e}\right)^4 \int_0^{\Theta_e/T} \frac{x^3}{e^x - 1}\,dx\right] \tag{50}$$

where $A(0)$ is the *hf* parameter extrapolated to $0K$, Θ_e is the effective Debye temperature and κ is a coupling constant. Fits to the low temperature values

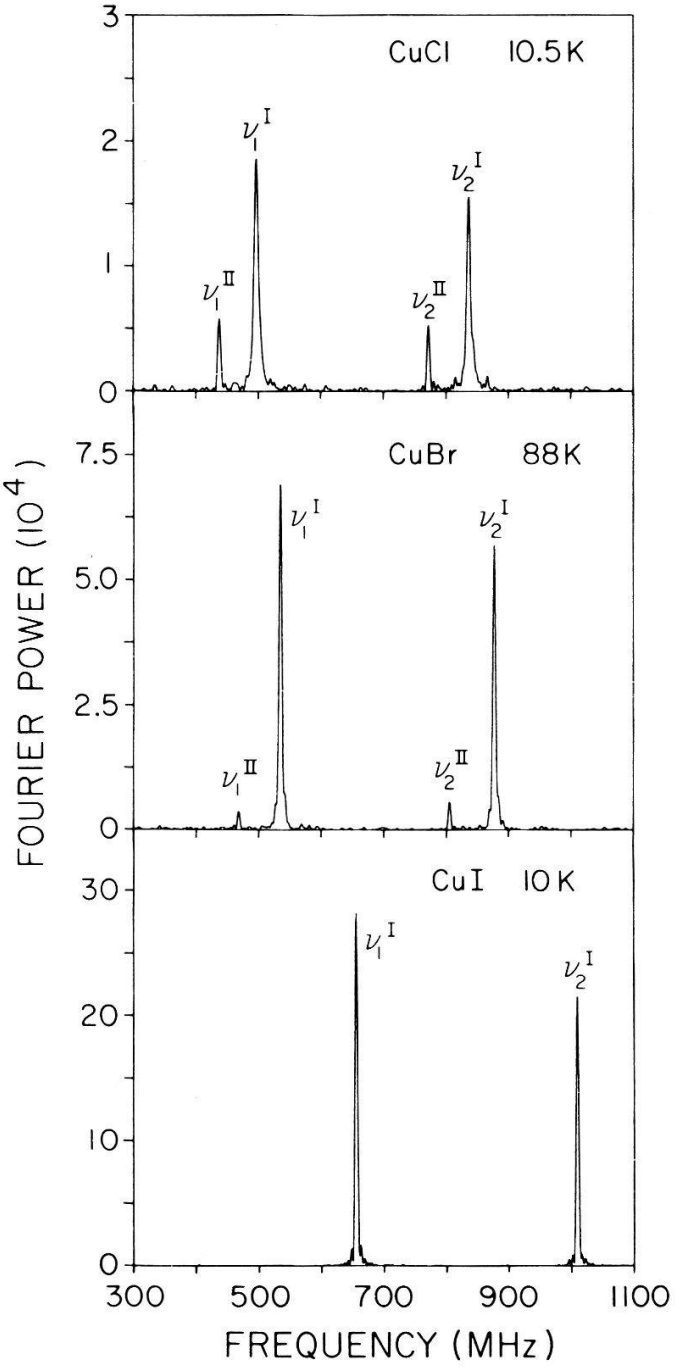

Figure 12
μSR spectra in the Cu halides in a transverse magnetic field of 1.156 T. In CuCl and CuBr, two distinct isotropic muonium centers (Mu^{I}, Mu^{II}) are observed.

(solid curves) and their extensions to higher temperatures (dashed curves) are plotted in Fig. 13. Note that for higher temperatures the data deviate systematically from the fitted Debye model. The fitted parameters are summarized in Table 4, together with the ratios of the electron and muon g factors obtained from the expression:

$$\frac{g_e}{g_\mu} = \frac{m_e}{m_\mu} \cdot \frac{2\nu_1\nu_2 + (\nu_1 + \nu_2)\nu_\mu}{\nu_\mu(\nu_1 + \nu_2 + 2\nu_\mu)} \tag{51}$$

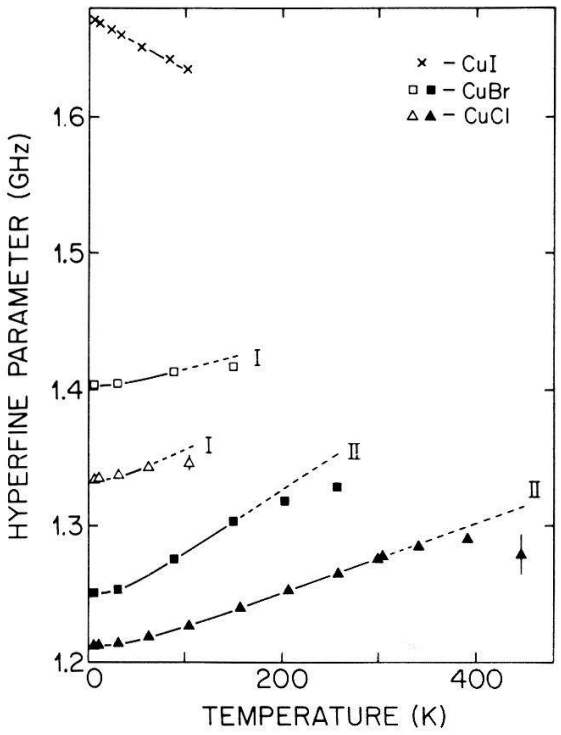

Figure 13
Measured *hf* frequencies of the isotropic muonium states in the Cu halides as function of temperature. The solid lines together with extrapolations to higher temperatures (dashed curves) were calculated using equation (50). The corresponding fit parameters are given in Table 4.

Note that the values of g_e/g_μ are 2–3% higher than for muonium in vacuum. The fitted Debye temperatures are compared with literature values Θ_D obtained from low-temperature specific heat data [51]. The observed value for Θ_e in CuI is approximately one order of magnitude less than the specific heat result.

At the highest temperatures, $A(T)$ for Mu^I and Mu^{II} in CuCl and CuBr appear to bend over. A similar non-monotonic behavior has been observed for Mu in silicon [5]. This has been attributed to the rapid hopping of Mu among two different sites with *hf* parameters differing by $\delta\nu_0$. The observed *hf* frequencies are then an average with the occupation of each site given by the Boltzmann factor. A fit to such a model fails for the Cu halides due to the limited data available.

Table 4
Debye model parameters as defined in equation (50) describing the low-temperature dependence of the *hf* parameter of Mu^I and Mu^{II} in the Cu halides. Debye temperatures Θ_D derived from specific-heat data are given for comparison, and the ratio between the electron and muon *g* factors for Mu^I at 5 K and for Mu^{II} at 150 K are also included.

Center	$A(0)$ (MHz)	κ	Θ_e (K)	Θ_D [a] (K)	g_e/g_μ [b]
Mu^I–CuCl	1334.24(7)	−0.083(75)	109(47)	164(4)	1.0292(40)
Mu^{II}–CuCl	1212.75(12)	−0.1016(23)	158(3)	164(4)	1.0335(36)
Mu^I–CuBr	1403.70(7)	−0.0470(82)	118(13)	161(2)	1.0207(15)
Mu^{II}–CuBr	1250.79(22)	−0.1311(88)	115(6)	161(2)	1.027(16)
Mu^I–CuI [b]	1670.94(23)	+0.0080(2)	11.4(2)	168(1)	1.0313(24)

[a]) Taken from Ref. 51.
[b]) Taken from Ref. 15.

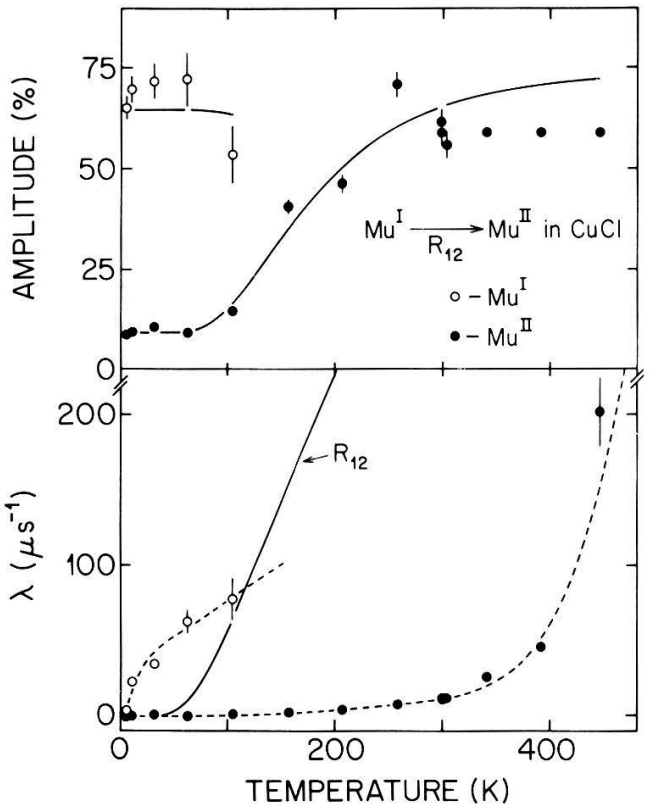

Figure 14
Normalized precession amplitudes and depolarization rates of the two isotropic muonium centers in CuCl as function of temperature. The behavior of the amplitudes indicates a $Mu^{I} \rightarrow Mu^{II}$ transition. The theoretical curves are described in the text.

It should be remembered that these copper halides are the least stable of all zincblende materials, implying that lattice expansion, anharmonic vibrational properties, or details of the acoustic phonon spectrum may be more important in the cuprous halides than in other materials. A further interesting point is the possibility that, with increasing temperature, the *hf* parameters for Mu^{I} and Mu^{II} approach or even cross one another. Such a crossing would have important consequences for a transition from Mu^{I} to Mu^{II}.

(b) *The thermally activated* $Mu^{I} \rightarrow Mu^{II} \rightarrow \mu^{+}$ *transition*

The temperature dependence of the precession amplitudes and depolarization rates of the CuCl Mu centers are shown in Fig. 14. The plotted amplitudes are the sum of the contributions from ν_1 and ν_2. Below 65 K, the amplitudes for both centers are temperature-independent, and the formation probability for Mu^{I} is approximately 7 times that for Mu^{II} (see Table 5). With account taken of the fraction precessing as bare muons, found to be 16(4)%, the resulting missing fraction for CuCl is 7.0(4.5)%.

With increasing temperature, the Mu^{I} signals become unobservable due to rapid depolarization. At higher temperatures, the Mu^{II} amplitude increases monotonically and at 250 K approaches the total low-temperature precession

Table 5
Model parameters describing the thermally-activated transitions from Mu^{I} to Mu^{II} to the bare muon state (μ^+). p_0^i, with $i = I - III$, are the formation probabilities for the Mu^{I}, Mu^{II} and the μ^+ state for $T > 700$ K, respectively. The transition rates Λ_{12} and Λ_{23} are assumed to follow an Arrhenius law (equation (46)) defined by the parameters ψ and U.

Method	p_0^{I} (%)	p_0^{II} (%)	p_0^{III} (%)	ψ_{12} (10^9 s^{-1})	U_{12} (meV)	ψ_{23} (10^9 s^{-1})	U_{23} (meV)
Weighted average:							
$T < 70$ K for Mu	67(8)	9.2(5)					
$T > 710$ K for μ^+			79(2)				
$Mu^{I} \rightarrow Mu^{II}$	64(2)	9.0(5)		0.88(15)	23(4)		
$Mu^{II} \rightarrow \mu^+$			84(4)			670(300)	256(19)

amplitude observed for both centers combined. Above room temperature, the Mu^{II} amplitude was fixed at the averaged room-temperature value of 58.7(1.8)% and is therefore plotted in Fig. 14 without error bars. The Mu^{II} depolarization rate increases slowly in the temperature region below 300 K, followed by a sharp increase above 370 K, and the state is unobservable above 445 K. The μ^+ amplitude plotted in Fig. 15 has been corrected for a contribution from the sample holder and oven walls by subtracting the low-temperature value of 34.5(3)%. Above 450 K, the free muon amplitude rises to a plateau value of

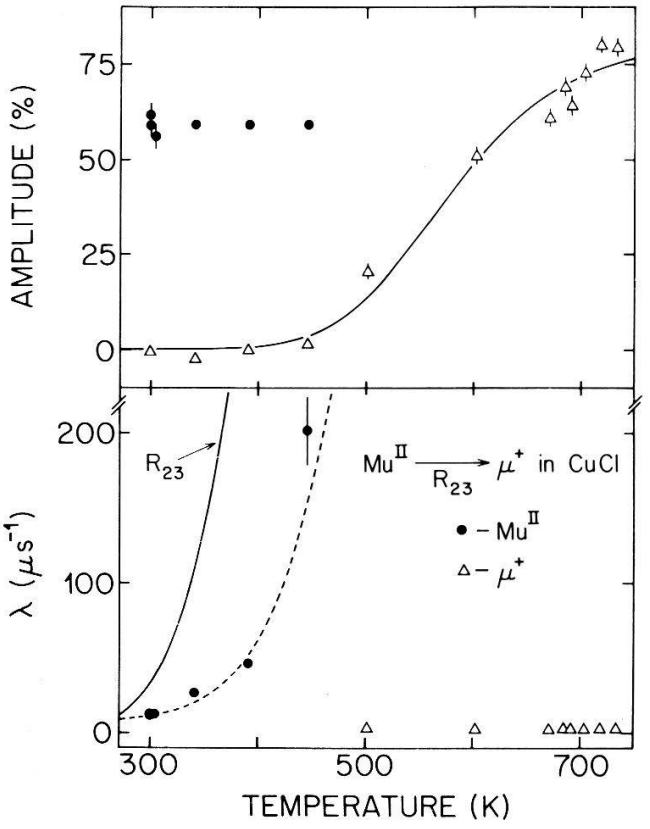

Figure 15
Normalized precession amplitudes and depolarization rates of the isotropic muonium center Mu^{II} and the diamagnetic center (μ^+) in CuCl as function of temperature. The behavior of the μ^+ signal strength indicates a $Mu^{II} \rightarrow \mu^+$ transition. The theoretical curves are described in the text.

76.7(1.4)% above 700 K. The depolarization rate of the bare muon remained approximately zero up to 733 K, the highest temperature investigated.

These facts strongly suggest the occurrence of a thermally-activated process of the form:

$$Mu^{I} \rightarrow Mu^{II} \rightarrow \mu^{+} \tag{52}$$

with corresponding transition rates Λ_{12} and Λ_{23}. Since the maxima in the amplitudes of Mu^{II} (at 250 K) and μ^{+} (at 700 K) are the same and approximately equal to the total low-temperature muonium amplitude, we may treat the two processes $Mu^{I} \rightarrow Mu^{II}$ and $Mu^{II} \rightarrow \mu^{+}$ separately.

1. *The transition from* Mu^{I} *to* Mu^{II}. The expressions for a $Mu^{I} \rightarrow Mu^{II}$ transition are obtained from equations (39–41) by setting $\Lambda_{21} = 0$. Since all measurements were performed in the high-field region, only the components at the frequencies ν_1 and ν_2 need be considered, and they have approximately the same amplitude. In the high-field limit the resulting expression for the Mu^{I} amplitude has the form:

$$a^{I} = p_0^{I} \cdot \left| \frac{-i\pi(\nu_0^{I} - \nu_0^{II})}{\Lambda_{12} - i\pi(\nu_0^{I} - \nu_0^{II})} \right| \tag{53}$$

and one obtains for the Mu^{II} amplitude:

$$a^{II} = \left| \frac{(p_0^{I} + p_0^{II})\Lambda_{12} - ip_0^{II}\pi(\nu_0^{I} - \nu_0^{II})}{\Lambda_{12} - i\pi(\nu_0^{I} - \nu_0^{II})} \right| \tag{54}$$

Here Λ_{12} is the transition rate, and p_0^{I} and p_0^{II} are the formation probabilities at early times, equal to the amplitudes in the absence of a transition. Below room temperature, results of a simultaneous fit of expressions of equations (53) and (54) to the available data are plotted in Fig. 14, assuming an Arrhenius law (equation (46)) for Λ_{12}. The fitted parameter values are summarized in Table 5. The formation probabilities are in good agreement with the averaged values found for low temperatures. The dashed curve in Fig. 14 is the predicted disappearance rate of Mu^{I} based on the rise of the Mu^{II} signal amplitude. Note that the low temperature values of Mu^{I} lie above the predicted curve and that their temperature-dependence is substantially different from a simple exponential behavior.

The Mu^{II} depolarization rate increases monotonically from approximately zero at 5 K to a room temperature value of 11.5(5) μs^{-1}. A fit of an Arrhenius-law to the data set up to room temperature leads to the parameter values:

$$\begin{aligned} \Psi &= 66.5(8.3)10^{6}\ s^{-1} \\ U &= 46.3(2.6)\ \text{meV} \end{aligned} \tag{55}$$

2. *The transition from* Mu^{II} *to the bare* μ^{+} *state.* Interesting effects may be expected for CuCl in the high-temperature region. The I–VII cuprous halides are

at the extreme ionic limit of the zincblende materials; all of them undergo a phase transition to the wurtzite structure at approximately the same temperature (680 K in CuCl). This phase change decreases the bonding coordination from four to three. The melting point of CuCl is at 695 K. To study the influence of these phase transitions on the muon states, we have extended our measurements of CuCl up to 733 K.

The free muon precession amplitude together with the Mu^{II} amplitude above 240 K is shown in Fig. 15. A monotonic increase in the μ^+ signal strength occurs directly above the temperature at which Mu^{II} disappears. The structural phase transition and the melting produce no significant change in the amplitude or depolarization rate of the μ^+ signal.

For a $Mu^{II} \rightarrow \mu^+$ transformation, the transition model predicts a time-dependent muon polarization in a high transverse field given by:

$$p_\mu(t) = p_0 \cos^2 \alpha \cdot \cos(\omega_\mu t) \tag{56}$$

with

$$\tan \alpha = -\frac{\pi \nu_0^{II}}{\Lambda_{23}} \tag{57}$$

Here Λ_{23} is the transition rate, which is assumed to follow an Arrhenius law. No temperature-independent 'prompt' μ^+ fraction is included. A temperature-independent *hf* parameter $\nu_0^{II} = 1300$ MHz has been assumed. The high-temperature μ^+ amplitude p_0 is constrained to be equal to the sum of the low-temperature Mu amplitudes $p_0^I + p_0^{II}$. The fitted parameters are given in Table 5. The fitted amplitudes (solid curve) and the predicted depolarization rate for Mu^{II} (dashed curve) are shown in Fig. 15.

Note that the observed Mu^{II} depolarization rates are *below* the predicted curve, in contrast to what is expected if channels other than the transformation exist for the depolarization of the precursor state. In nitrogen-rich diamond, for example, Mu trapping at impurities makes the observation of Mu impossible above 150 K, whereas the present measurements on the type-IIb stone show Mu signals up to 400 K. Note, however that since the transferred μ^+ amplitude in CuCl depends on the temperature-dependent Mu^{II} *hf* frequency $A(T)$ (see equation (57)), an extrapolation of this parameter to temperatures above the highest temperature observation of Mu^{II} is necessary. By assuming that A *decreases* with increasing temperature above 445 K the rise in the μ^+ amplitude can be explained with a *lower* transition rate Λ_{23}. A fit was performed under the assumption that the transition rate Λ_{23} is equal to the observed temperature-dependent Mu^{II} depolarization rate. The Mu^{II} *hf* frequency, taken to be temperature-independent, and the fraction $p(0)$ were allowed to vary. The fitted Mu^{II} *hf* frequency temperatures was 186(11) MHz, approximately $\frac{1}{6}$ of the 0 K value of 1213 MHz. The transferred muon fraction $p(0)$ was again 82(2)%, in good agreement with the values listed in Table 5.

(c) *Discussion*

With the high field, high timing resolution apparatus, we have observed two distinct isotropic muonium centers Mu^{I} and Mu^{II} in CuCl and CuBr, with *hf* frequencies approximately $\frac{1}{3}$ of the vacuum value. The *hf* parameters for both Mu centers in CuCl and CuBr generally increase with increasing temperature – in contrast to the behavior for the Mu centers observed in other semiconductors. In CuI, only one Mu center is observed, with a *hf* parameter which decreases with increasing temperature. An isotropic *hf* interaction implies that state occupies a site with high symmetry or that the center is rapidly diffusing between lower-symmetry sites, averaging out the anisotropy. The latter possibility is ruled out by the observation of Kiefl et al. [15] that, with the possible exception of Mu^{I} in CuCl below 10.5 K, no motional averaging of the Mu nuclear hyperfine interaction occurs in any Cu halide (all the host nuclei in these materials have spin). These authors proposed instead that Mu^{I} and Mu^{II} occupy the two inequivalent tetrahedral interstitial sites.

All the Mu centers in CuCl become unstable at the temperature at which the *hf* coupling constant reaches a broad maximum. With increasing temperature, first the Mu^{I} centers become unstable, undergoing a thermally-activated transition to Mu^{II}. At still higher temperatures, the Mu^{II} center in CuCl also becomes unstable and makes a transition to the diamagnetic state μ^{+}.

Since the Mu^{II} state is affected directly by both transition processes, an appropriate model to describe its temperature-dependent amplitude is one which includes *both* transition rates Λ_{12} and Λ_{23}. A fit to such a model fails for several reasons: i) the highest-temperature signals observed from the Mu^{I} state are at 100 K, whereas the increase in the free muon signal strength occurs at temperatures above 450 K, and an extrapolation of the temperature-dependent Mu^{I} *hf* parameter to this temperature is questionable. ii) extrapolation of the *hf* parameters to temperatures above 450 K could lead to a crossover of the Mu^{I} and Mu^{II} *hf* frequencies, resulting in a resonance effect for the Mu^{II} amplitude. The available data show no evidence for such behavior.

Neither Mu depolarization rate can be explained by a simple exponential. The assumption of a second depopulation process for Mu^{I}, for example a transition $Mu^{I} \rightarrow \mu^{+}$ with a rate Λ_{13}, leads to a Mu^{I} depolarization rate which is equal to the sum $\Lambda_{12} + \Lambda_{13}$. The test of such a model will require more data. The

Table 6
Parameters describing the temperature dependence of the depolarization rate of the Mu^{I} and Mu^{II} center in CuCl as a sum of two Arrhenius laws. This behavior is predicted if an additional depolarization process is assumed. The corresponding curves (dot-dashed) are shown in Fig. 14 and Fig. 15.

	Ψ_1 ($10^6\,s^{-1}$)	U_1 (meV)	Ψ_2 ($10^6\,s^{-1}$)	U_2 (meV)
Mu^{I} depolarization rate:	70	1.35	180	20
Mu^{II} depolarization rate:	53	42.7	1.4×10^6	355

dot-dashed curves plotted in Figs. 14 and 15 were obtained from the sum of two Arrhenius curves with the parameters given in Table 6, and are only intended to guide the eye.

VI. Thermally-activated transitions in high-purity silicon

(a) *The* $\mathrm{Mu} \leftrightarrow \mu^+$ *transition above* 240 *K*

As in diamond [2], three different muon states, Mu, Mu* and μ^+, are seen in high-purity silicon at temperatures below 100 K. Data on the temperature-dependent muonium dynamics obtained from measurements on various samples [5, 27, 52–55] are presented in Fig. 16. At the lowest temperatures only a small μ^+ fraction is seen, together with the Mu* and Mu fractions indicated by the arrows in the third section of the figure. As the temperature is increased, first the Mu* state becomes unstable, as indicated by its increasing depolarization rate λ_{Mu^*}. The subsequent rise in the μ^+ amplitude a_{μ^+} indicates that a $\mathrm{Mu}^* \rightarrow \mu^+$ transition occurs. Next the Mu state becomes unstable, also ending up as μ^+. At the highest temperatures yet studied, even the μ^+ appears to become unstable. Since not only the μ^+ amplitude, but also its depolarization rate increases for temperatures over 400 K, a simple transition model $\mathrm{Mu} \rightarrow \mu^+$ fails to describe the data.

The normalized precession amplitudes and depolarization rates of the Mu and μ^+ states at high-temperatures in a transverse field of 106 G are shown in Fig. 17. The plotted total Mu amplitude has been corrected for the finite time-resolution of the μSR apparatus. For temperatures above 240 K, the $\mathrm{Mu}^* \rightarrow \mu^+$ transition is already complete, leading to an enhanced μ^+ amplitude of 45.86(55)%. The Mu amplitude was found to be 61.5(2.6)% and was held fixed during the analysis of the muonium depolarization rates. The small μ^+ background signal from the cryostat and oven were taken into account.

In order to consistently describe the μ^+ and Mu data, we propose that a reversible transition, $\mathrm{Mu} \leftrightarrow \mu^+$, between the Mu and the μ^+ states occurs. The spin dynamics for such a process is described by equations (19, 20) with Λ_{12} and Λ_{21} representing the rates for the processes $\mathrm{Mu} \rightarrow \mu^+$ and $\mu^+ \rightarrow \mathrm{Mu}$, respectively. Use of the reduced differential equation set given in the Appendix (equations (A3, A4)) simplifies the problem. We then obtain 5 coupled differential equations which cannot be solved analytically. Although information on the temperature-dependence of the *hf* parameter $A(T)$ for Mu in Si is available from [5], it is not needed for a description of the total Mu amplitude, given by $2(a_{12} + a_{23})$, since this sum is independent of A.

A combined fit of the precession amplitudes and depolarization rates of Mu and μ^+ state to the transition model $\mathrm{Mu} \leftrightarrow \mu^+$ is plotted in Fig. 17. The fitted Arrhenius parameters for the transition rates are summarized in Table 7. Below room-temperature, the $\mathrm{Mu} \rightarrow \mu^+$ transition at the rate Λ_{12} is dominant, with an almost negligible effect from Λ_{21}. Above 600 K the μ^+ depolarization rate is

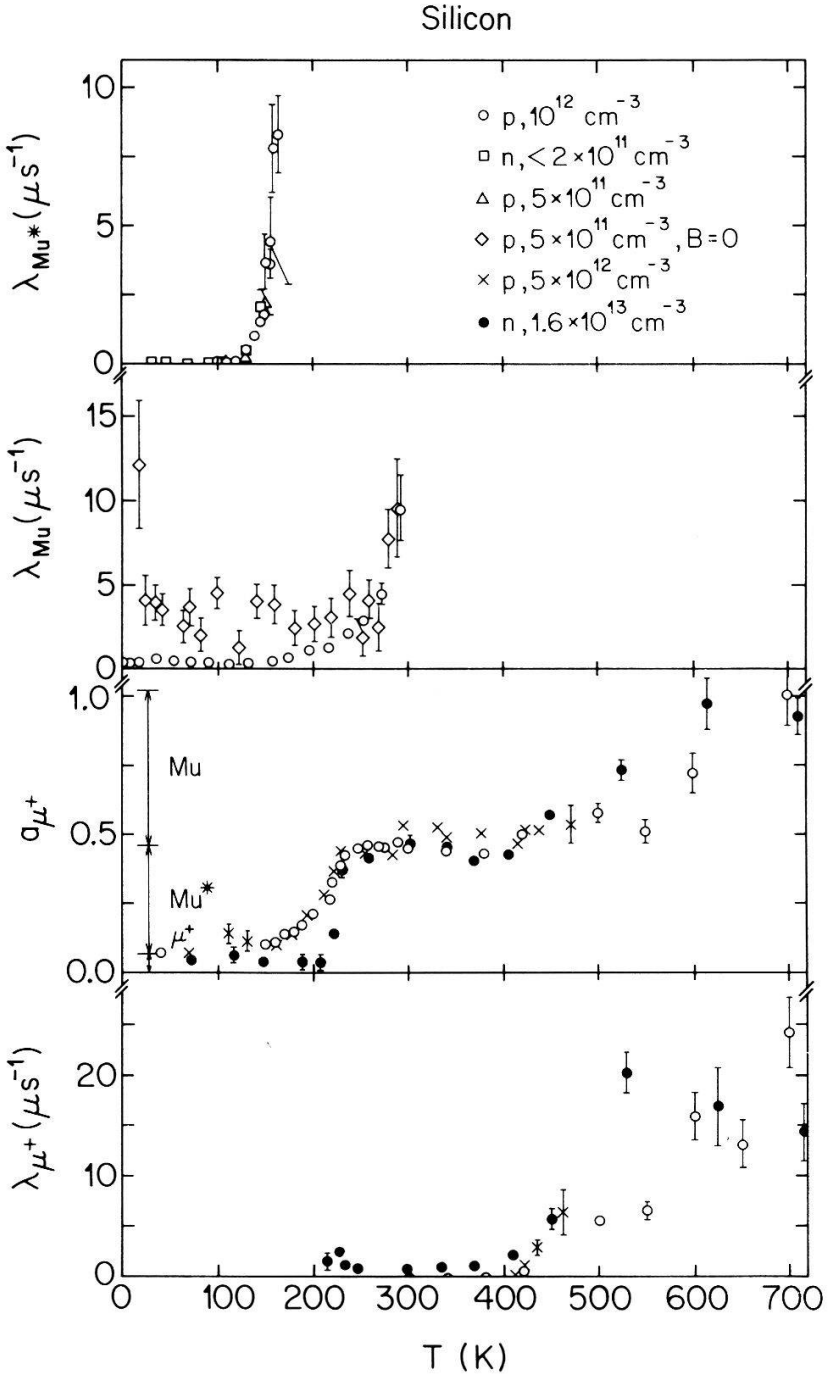

Figure 16
Collected data on muonium dynamics in various high-purity silicon samples: p, $10^{12}\,cm^{-3}$ [52]; n, $<2\times10^{11}\,cm^{-3}$ [53]; p, $5\times10^{11}\,cm^{-3}$ [27]; p, $5\times10^{11}\,cm^{-3}$, $B=0$ [5]; p, $5\times10^{12}\,cm^{-3}$ [54]; n, $1.6\times10^{13}\,cm^{-3}$ [55].

approximately half the Λ_{21} transition rate. A basic property of a reversible process is the appearance of a shift in the precession frequencies for high transition rates. We compare the predicted μ^+ frequency shift based on the fitted Arrhenius parameters with the observed frequency shift in Fig. 17. The consistent explanation of the amplitudes, relaxation rates and μ^+ frequency shift are strong evidence for the reversible Mu $\leftrightarrow \mu^+$ transition model.

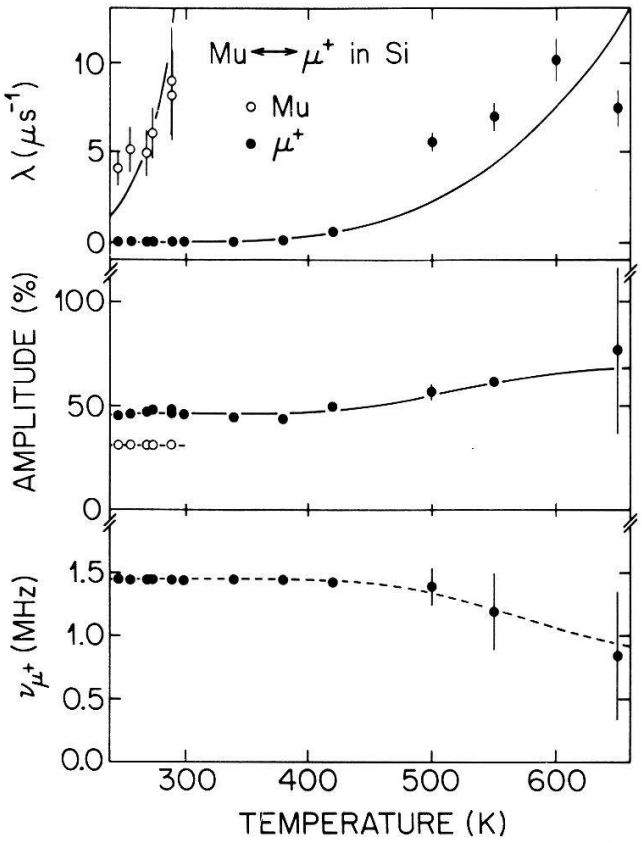

Figure 17
Temperature dependence of the Mu and μ^+ amplitudes and depolarization rates measured for a $10^{12}\,\mathrm{cm}^{-3}$ (p-type) silicon sample in a field of 1.1 mT. The solid curves are fits to the Mu $\leftrightarrow \mu^+$ transition model. Also shown is the predicted μ^+ frequency shift ν_{μ^+} (dashed curve) together with the corresponding experimental data.

(b) *The* Mu* $\rightarrow \mu^+$ *transition*

As mentioned above, the Mu* state in Si is unstable above 150 K and is no longer observable above 165 K. The rise in the μ^+ amplitude above 150 K indicates that a Mu* $\rightarrow \mu^+$ transition occurs. Since no related increase of the μ^+ relaxation rate is observed, the transition is believed to be irreversible.

In the absence of additional depolarization, such as from the scattering of

Table 7
Model parameters describing the thermally-activated transitions Mu $\leftrightarrow \mu^+$ and Mu* $\rightarrow \mu^+$ observed in high-purity silicon. The fitted Mu and μ^+ Arrhenius parameters (equation (46)) are based on a Mu $\leftrightarrow \mu^+$ transition, and the Mu* parameters are from fits of the Mu* depolarization rates to an Arrhenius law. The fraction and Arrhenius parameters specified for a particular state refer to the amount of muon polarization transferred *from* the state indicated and the rate at which this state is depleted.

	Mu*	Mu	μ^+
fraction $p(0)$ (%)	39.0(1.4)	61.5(2.6)	6.75(23)
Ψ ($10^9\,\mathrm{s}^{-1}$)	948(71)	197(52)	21(5)
U (meV)	167(9)	246(8)	386(9)

free carriers by Mu*, the Mu* damping rate of the precursor Mu* state is equal to the Mu$\rightarrow\mu^+$ transition rate Λ. The temperature dependence of the Mu* relaxation rate was studied in the range of 100 K to 200 K in an applied field of 29 mT [56]. A fit of the Mu* relaxation rate to an Arrhenius law (equation (46)) leads to the parameter values listed in Table 7.

The sample was oriented with the $\langle 110\rangle$ axis perpendicular to the external field, and an analysis of the Mu* frequencies at 40 K yielded the following angles between the field and the Mu* symmetry axes: 103.7° (two states), 120.5° and 11°. Since analytical solutions for isolated Mu* are only available for $\vec{n}\perp\vec{B}$ or $\vec{n}\parallel\vec{B}$, the transition problem must be solved numerically. With the polarization simultaneously transferred from all four Mu* centers at the same rate $\Lambda(T)$, and including the Mu$\leftrightarrow\mu^+$ process, the dimension of the matrix to be diagonalized is 78 (see equation (23–25)). The large computing effort made fitting impractical.

The observed μ^+ amplitude at 10.6 and 287.1 mT as function of temperature in the range 100 K to 300 K are shown in Fig. 18 together with the model calculations based on the transition rate $\Lambda(T)$. The prompt formation probability for μ^+, taken from measurements at 150 K and 287.1 mT, is 6.83(23)%, and that of the Mu* state was taken to be the difference 39.0(1.4)% between the μ^+ amplitude in the range 275–400 K and this value.

The agreement between experiment and theory is encouraging. The fact that the predicted rise in a_{μ^+} occurs at a higher temperature than that observed is

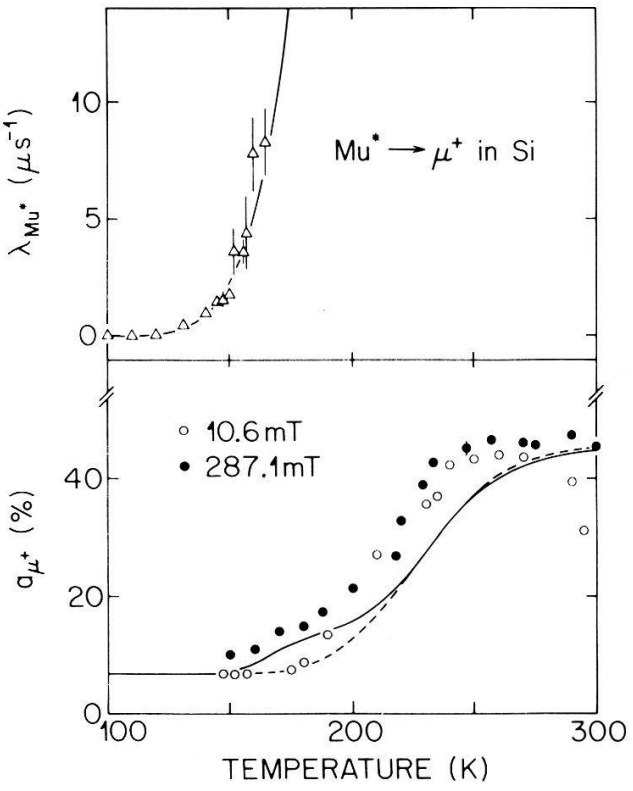

Figure 18
The thermally-activated Mu*$\rightarrow\mu^+$ transition observed in Si. The dot-dashed curve is a fit of an Arrhenius law to the Mu* depolarization rate. The solid line is a theoretical calculation based on the transition model described in the text.

reminiscent of the case $Mu^{II} \rightarrow \mu^+$ in CuCl, and, as discussed there, may indicate a sharp decrease in the Mu* *hf* frequency above 160 K. The different behavior of the μ^+ amplitude for the two fields appears to be well-represented. Not understood at the moment are the low values of the μ^+ amplitude for 287.1 mT above 270 K. A possible explanation is an interference effect between the two processes $Mu^* \rightarrow \mu^+$ and $Mu \leftrightarrow \mu^+$.

(c) *Discussion*

As discussed in Section IV, the thermally-activated transition from Mu to Mu* in diamond allows an experimental determination of the sign of the Mu* *hf* coupling constants A_s and A_p, relative to the Mu *hf* coupling constant A(Mu). In *electron-irradiated* silicon no Mu signal is observed [57], implying that Mu is diffusing and becoming trapped at radiation defect centers. At the applied field where the Mu and Mu* frequencies coincide, a resonant transfer of the muon polarization from Mu to Mu* is observed, but the resonance is too broad to permit a determination of the sign of the Mu* hyperfine coupling constants.

In high-purity silicon, two transitions occur. In the temperature range 120–250 K, Mu* makes a transition to the μ^+ state. Above 200 K, one finds that the Mu state undergoes a reversible $Mu \leftrightarrow \mu^+$ transition. The increase in the Mu* and Mu depolarization rates and the subsequent rises in the μ^+ amplitude and relaxation rate with increasing temperature can be accounted for using the transition model. A sign determination of the Mu* *hf* parameters is not possible using the $Mu^* \rightarrow \mu^+$ because the bound electron is lost during the reaction and therefore, in contrast to the case of diamond, no selection rules for the polarization transfer.

VII. Conclusions

Thermally-activated transitions among the various muon states were investigated in the elemental semiconductors silicon and diamond and in the compound semiconductors CuCl, CuBr and CuI. In this Paper, a general theory was developed which describes the spin dynamics of irreversible and reversible transitions among an arbitrary number of different muon states and which can treat the conservation or loss of the electron polarization. The results obtained can be quantitatively described using the theory.

Our study of the Mu to Mu* transition in type-IIb diamond establishes that the isotropic part of the Mu* hyperfine interaction is *negative*. This implies that Mu* is not simply a distorted version of isotropic Mu, since this would require a positive hyperfine interaction. Instead, it is a paramagnetic complex similar to a molecular radical with the unpaired electron removed from the muon. The weak negative spin density at the muon is then the result of an exchange polarization mechanism. Among the models for the Mu* state, the relaxed bond-center model

is at present the leading contender. It is supported both by the 'Level-Crossing-Resonance' measurements of the Mu* nuclear hyperfine interaction in silicon [49] and GaAs [50], and by cluster calculations [46, 48]. The large Arrhenius prefactor Ψ for the transition rate excludes a model where Mu hops around in the lattice and finds an existing lattice-ion vacancy, where it becomes trapped as Mu*. Isotropic Mu is believed to be located at or near an interstitial site in the diamond lattice [31–38].

For all the investigated transitions, the assumption of an Arrhenius law for the temperature-dependent reaction rate $\Lambda(T)$ is supported by the data. In diamond, a single Arrhenius-law describes the $\mathrm{Mu} \rightarrow \mathrm{Mu}^*$ reaction over more than 5 orders of magnitude in Λ. The prediction of the theory is verified that, in the absence of additional depolarization mechanisms, the depolarization rate for an irreversible process is equal to the transition rate. Measurements on a nitrogen-rich diamond [2] show that rapid Mu relaxation, presumably due to impurity trapping, reduces the maximum possible temperature of Mu observation from 400 K to 150 K. The observation of a $\mathrm{Mu} \leftrightarrow \mu^+$ process in Si establishes that a rapid, reversible transition among muon states leads to a shift in the precession frequencies. A further conclusion drawn from our investigations on diamond and CuCl is that the electron spin is conserved during the transition from one paramagnetic muonium state to another.

The measurements performed on CuCl above 500 K show no appreciable effect of the structural phase transition or the sample melting on the μSR signals. At low temperatures, the *hf* coupling constants for both muonium centers in CuCl and CuBr generally increase with increasing temperature – opposite to what is observed for isotropic muonium centers in other semiconductors [3]. This may be related to the marginal stability of these materials [26, 58].

Acknowledgements

I would like to thank everyone who has helped with this work. Special thanks are due to Professor Walter Kündig and Bruce Patterson, who have stimulated this work and without whom it would have been impossible. I also wish to thank Hugo Keller for critical reading of the manuscript, and Prof. P. F. Meier and M. Celio for stimulating discussions. Assistance from the other group members R. F. Kiefl, Hp. Baumeler, J. W. Schneider, H. Simmler and I. Savic (University of Belgrade) was greatly appreciated. The diamond experiments were supported by J. P. F. Sellschop, M. C. Stemmet and S. Connell (University of the Witwatersrand, Johannesburg), who supplied the high-purity diamond. The copper halide crystals were supplied by C. Schwab (Université Louis Pasteur, Strasbourg). I would like to thank the Swiss Institute for Nuclear Research (SIN) for its technical assistance and the Swiss National Science Foundation, who has supported this work.

Appendix

In this appendix reduced set of differential equations treating the time dependent muon polarization in the Mu* state are listed.

Following Ivanter and Smilga [17] and Brewer et al. [22], we introduce new vectors $\vec{P}$ and new matrices M (see equations (13) and (14)) to obtain reduced set of coupled differential equations. In the following section, the expressions for $\vec{P}$ and M are summarized for $\vec{n} \perp \vec{B}$ and $\vec{n} \parallel \vec{B}$ with respect to the longitudinal and transversal subsystem.

(1) Mu* with $\vec{n} \parallel \vec{B} \parallel z$-axis

(1.1) Longitudinal subsystem

$$\vec{P} = \begin{pmatrix} p_\mu^3 \\ p_e^3 \\ p^{11} + p^{22} \\ p^{12} - p^{21} \end{pmatrix} \tag{A1}$$

$$M = \begin{pmatrix} 0 & 0 & 0 & -\frac{1}{2}\omega_0 \\ 0 & -2\nu_{ex} & 0 & \frac{1}{2}\omega_0 \\ 0 & 0 & -2\nu_{ex} & -(\omega_e + \omega_\mu) \\ \omega_0 & -\omega_0 & (\omega_e + \omega_\mu) & -2\nu_{ex} \end{pmatrix} \tag{A2}$$

(1.2) Transversal subsystem

$$\vec{P} = \begin{pmatrix} p_\mu^1 + ip_\mu^2 \\ p_e^1 + ip_e^2 \\ p^{13} + ip^{23} \\ p^{31} + ip^{32} \end{pmatrix} \tag{A3}$$

$$M = \begin{pmatrix} -i\omega_\mu & 0 & \frac{i}{2}(\omega_0 + \omega^*) & -\frac{i}{2}\omega_0 \\ 0 & i\omega_e - 2\nu_{ex} & -\frac{i}{2}\omega_0 & \frac{i}{2}(\omega_0 + \omega^*) \\ \frac{i}{2}(\omega_0 + \omega^*) & -\frac{i}{2}\omega_0 & -i\omega_\mu - 2\nu_{ex} & 0 \\ -\frac{i}{2}\omega_0 & \frac{i}{2}(\omega_0 + \omega^*) & 0 & i\omega_e - 2\nu_{ex} \end{pmatrix} \tag{A4}$$

(2) Mu* with $\vec{n} \perp \vec{B} \parallel z$-axis

It is convenient to introduce β, the angle between the x-axis and $\vec{n}$. Then we can write $\vec{n} = (\cos\beta, \sin\beta, 0)$.

(2.1) Longitudinal subsystem

$$\vec{P} = \begin{pmatrix} p_\mu^3 \\ p_e^3 \\ p^{11} \\ p^{22} \\ p^{12} \\ p^{21} \end{pmatrix} \tag{A5}$$

$$M = \frac{1}{2} \begin{pmatrix} 0 & 0 & -\omega^* n_1 n_2 \\ 0 & -4\nu_{ex} & -\omega^* n_1 n_2 \\ \omega^* n_1 n_2 & \omega^* n_1 n_2 & -4\nu_{ex} \\ -\omega^* n_1 n_2 & -\omega^* n_1 n_2 & 0 \\ (\omega_0 + \omega^* n_2^2) & -(\omega_0 + \omega^* n_1^2) & 2\omega_e \\ -(\omega_0 + \omega^* n_1^2) & (\omega_0 + \omega^* n_2^2) & -2\omega_\mu \end{pmatrix}$$

$$\begin{pmatrix} \omega^* n_1 n_2 & -(\omega_0 + \omega^* n_2^2) & (\omega_0 + \omega^* n_1^2) \\ \omega^* n_1 n_2 & (\omega_0 + \omega^* n_1^2) & -(\omega_0 + \omega^* n_2^2) \\ 0 & -2\omega_e & 2\omega_\mu \\ -4\nu_{ex} & -2\omega_\mu & 2\omega_e \\ 2\omega_\mu & -4\nu_{ex} & 0 \\ -2\omega_e & 0 & -4\nu_{ex} \end{pmatrix} \tag{A6}$$

(2.2) Transversal subsystem

$$\vec{P} = \begin{pmatrix} p_\mu^1 + ip_\mu^2 \\ p_e^1 + ip_e^2 \\ p^{13} + ip^{23} \\ p^{31} + ip^{32} \\ p_\mu^1 - ip_\mu^2 \\ p_e^1 - ip_e^2 \\ p^{13} - ip^{23} \\ p^{31} - ip^{32} \end{pmatrix} \tag{A7}$$

$$A = \begin{pmatrix} -i\omega_\mu & 0 & \frac{i}{2}\omega_0 & -\frac{i}{2}(\omega_0 + \frac{1}{2}\omega^*) \\ 0 & i\omega_e - 2\nu_{ex} & -\frac{i}{2}(\omega_0 + \frac{1}{2}\omega^*) & \frac{i}{2}\omega_0 \\ \frac{i}{2}\omega_0 & -\frac{i}{2}(\omega_0 + \frac{1}{2}\omega^*) & -i\omega_\mu - 2\nu_{ex} & 0 \\ -\frac{i}{2}(\omega_0 + \frac{1}{2}\omega^*) & \frac{i}{2}\omega_0 & 0 & i\omega_e - 2\nu_{ex} \end{pmatrix} \tag{A8}$$

$$C = i\frac{\omega^*}{4}\exp[-2i\beta] \cdot \begin{pmatrix} & & & 1 \\ & & 1 & \\ & -1 & & \\ -1 & & & \end{pmatrix} \tag{A9}$$

$$M = \begin{pmatrix} A & C^* \\ C & A^* \end{pmatrix} \tag{A10}$$

The failure to reduce the problem to four dimensions is due to the fact that in general p_μ^1 and p_μ^2 are no longer separated by the phase $\pi/2$. If one is only interested in either p_μ^1 or p_μ^2, such a reduction can be achieved.

REFERENCES

[1] B. D. PATTERSON, in *Muons and Pions in Materials Research*, edited by J. Chappert and R. I. Grynszpan (North Holland, Amsterdam/Oxford/New York/Tokyo) p. 161 (1984).
[2] E. HOLZSCHUH, W. KÜNDIG, P. F. MEIER, B. D. PATTERSON, J. P. F. SELLSCHOP, M. C. STEMMET, and H. APPEL, Phys. Rev. A *25*, 1272 (1982).
[3] B. D. PATTERSON, submitted to Rev. Mod. Phys.
[4] J. CHAPPERT and R. I. GRYSZPAN, *Muons and Pions in Material Research*, North-Holland, Amsterdam, Oxford, New York, Tokyo, (1984).
[5] E. HOLZSCHUH, Phys. Rev. B *27*, 102 (1983).
[6] J. H. BREWER, K. M. CROWE, F. N. GYGAX, R. F. JOHNSON, B. D. PATTERSON, D. G. FLEMING, and A. SCHENCK, Phys. Rev. Lett. *31*, 143 (1973).
[7] B. D. PATTERSON, A. HINTERMANN, W. KÜNDIG, P. F. MEIER, F. WALDNER, H. GRAF, E. RECKNAGEL, A. WEIDINGER, and Th. WICHERT, Phys. Rev. Lett. *40*, 1347 (1978).
[8] E. HOLZSCHUH, H. GRAF, E. RECKNAGEL, A. WEIDINGER, Th. WICHERT, and P. F. MEIER, Phys. Rev. B *20*, 4391 (1979).
[9] R. F. KIEFL, J. W. SCHNEIDER, H. KELLER, W. KÜNDIG, W. ODERMATT, P. D. PATTERSON, K. W. BLAZEY, T. L. ESTLE, and S. L. RUDAZ, Phys. Rev. B *32*, 530 (1985).
[10] A. ABRAGAM and B. BLEANEY, *Electron Paramagnetic Resonance of Transitions Ions* (Clarendon, Oxford, 1970), p. 260.
[11] P. F. MEIER, Phys. Rev. A *25*, 1287 (1982).
[12] J. W. SCHNEIDER, Hp. BAUMELER, H. KELLER, R. F. KIEFL, W. KÜNDIG, W. ODERMATT, and B. D. PATTERSON, Hyperfine Interact. *32*, 607 (1986).
[13] B. D. PATTERSON, E. HOLZSCHUH, W. KÜNDIG, P. F. MEIER, W. ODERMATT, J. P. F. SELLSCHOP, and M. C. STEMMET, Hyperfine Interact. *17–19*, 605 (1984).

[14] W. Odermatt, Hp. Baumeler, H. Keller, W. Kündig, B. D. Patterson, J. W. Schneider, J. P. F. Sellschop, M. C. Stemmet, S. Connell, and D. P. Spencer, Phys. Rev. B. (in press).
[15] R. F. Kiefl, W. Odermatt, Hp. Baumeler, J. Felber, H. Keller, W. Kündig, P. F. Meier, B. D. Patterson, J. W. Schneider, K. W. Blazey, T. L. Estle, and C. Schwab, Phys. Rev. B *34*, 1474 (1986).
[16] E. Rapport and C. W. F. T. Pistorius, Phys. Rev. *172*, 838 (1968).
[17] I. G. Ivanter and V. P. Smilga, Zh. Eksp. Teor. Fiz. *54*, 559 (1968) [Sov. Phys. -JETP *27*, 301 (1968)].
[18] P. W. Percival and H. Fischer, Chem. Phys. *16*, 89 (1976).
[19] E. Roduner and H. Fischer, Chem. Phys. *54*, 261 (1981).
[20] M. Celio, private communication.
[21] Yu. M. Belousov, V. N. Gorelkin and V. P. Smilga, Zh. Eksp. Teor. Fiz. *81*, 642 (1981) [Sov. Phys. JEPT *54*, 343 (1981)]
[22] C. S. Wu and V. W. Hughes, In *Muon Physics III, Chemistry and Solids* edited by V. W. Hughes and C. S. Wu (Academic, New York, 1976), p. 40.
[23] H. Fischer and H. Paul, Acc. Chem. Research *20*, 200 (1987).
[24] A. B. Denison, H. Graf, W. Kündig and P. F. Meier Helv. Phys. Acta *52*, 460 (1979).
[25] R. F. Kiefl, E. Holzschuh, H. Keller, W. Kündig, P. F. Meier, P. D. Patterson, J. W. Schneider, K. W. Blazey, S. L. Rudaz, and A. B. Denison, Phys. Rev. Lett. *53*, 90 (1984).
[26] C. Schwab, and A. Goltzené, Prog. Cryst. Growth Charact. *5*, 233 (1982).
[27] K. W. Blazey, J. A. Brown, D. W. Cooke, S. A. Dodds, T. L. Estle, R. H. Heffner, M. Leon and D. A. Vanderwater, Phys. Rev. B *23*, 5316 (1981).
[28] K. W. Blazey, T. L. Estle, E. Holzschuh, W. Odermatt, and B. D. Patterson Phys. Rev. B *27*, 15 (1983).
[29] A. Weidinger, G. Balzer, H. Graf, E. Recknagel, and Th. Wichert, Phys. Rev. B *24*, 6185 (1981).
[30] E. Albert, A. Möslang, E. Recknagel, and A. Weidinger, Hyperfine Interact. *17–19*, 611 (1984).
[31] M. Manninen and P. F. Meier, Phys. Rev. B *26*, 6690 (1982).
[32] N. Sahoo, S. K. Mishra, A. Coker, T. P. Das, C. K. Mitra, L. C. Snyder, and A. Glodeanu, Phys. Rev. Lett. *50*, 913 (1983).
[33] H. Katayama-Yoshida and K. Shindo, Phys. Rev. Lett. *51*, 207 (1983).
[34] S. Estreicher, A. K. Ray, J. L. Fry and D. S. Marynick, Phys. Rev. Lett. *55*, 1976 (1985).
[35] S. Estreicher and D. S. Marynick, Hyperfine Interact. *32*, 613 (1986).
[36] S. Estreicher, A. K. Ray, J. L. Fry and D. S. Marynick, Phys. Rev. B *34*, 6071 (1986).
[37] N. Sahoo, K. C. Mishra and T. P. Das, Phys. Rev. Lett. *57*, 3300 (1986).
[38] S. Estreicher, A. K. Ray, J. L. Fry and D. S. Marynick, Phys. Rev. Lett. *57*, 3301 (1986).
[39] T. L. Estle, Hyperfine Interact. *17–19*, 585 (1984).
[40] N. Sahoo, K. C. Mishra, and T. P. Das, Phys. Rev. Lett. *55*, 1506 (1985).
[41] S. Estreicher and D. S. Marynick, Phys. Rev. Lett. *56*, 1511 (1986).
[42] N. Sahoo, K. C. Mishra, and T. P. Das, Phys. Rev. Lett. *56*, 1512 (1986).
[43] N. Sahoo, K. C. Mishra, and T. P. Das, Hyperfine Interact. *32*, 619 (1986).
[44] M. C. R. Symons, Hyperfine Interact. *17–19*, 771 (1984).
[45] S. F. J. Cox and M. C. R. Symons, Chem. Phys. Lett. *126*, 516 (1986).
[46] T. A. Claxton, A. Evans, and M. C. R. Symons, J. Chem. Soc., Faraday Trans. 2 *82*, 2031 (1986).
[47] T. L. Estle, S. Estreicher, and D. S. Marynick, Hyperfine Interact. *32*, 637 (1986).
[48] T. L. Estle, S. Estreicher, and D. S. Marynick, Phys. Rev. Lett. *58*, 1547 (1987).
[49] R. F. Kiefl, M. Celio, T. L. Estle, S. R. Kreitzman, G. M. Luke, T. M. Riseman, and E. J. Ansaldo, Phys. Rev. Lett. *60*, 224 (1988).
[50] R. F. Kiefl, M. Celio, T. L. Estle, G. M. Luke, S. R. Kreitzman, J. H. Brewer, D. R. Noakes, E. J. Ansaldo, and K. Nishiyama, Phys. Rev. Lett. *58*, 1780 (1987).
[51] Z. Vardeny, G. Gilat and D. Moses, Phys. Rev. B *18*, 4487 (1978).
[52] B. D. Patterson, E. Holzschuh, R. F. Kiefl, K. W. Blazey and T. L. Estle, Hyperfine Interact. *17–19*, 599 (1984).
[53] E. Albert, A. Möslang, E. Recknagel and A. Weidinger, Hyperfine Interact. *17–19*, 611 (1984).

[54] S. G. BARSOV et al. Zh. Eksp. Teor. Fiz. *79*, 1461 (1980) [Sov. Phys. JETP *52*, 738 (1980)].
[55] S. G. BARSOV et al. Zh. Eksp. Teor. Fiz. *76*, 2198 (1979) [Sov. Phys. JETP *49*, 1110 (1979)].
[56] H. SIMMLER, Ph. D. Thesis, University of Zürich, 1987.
[57] E. WESTHAUSER, E. ALBERT, M. HAMMA, E. RECKNAGEL, and A. WEIDINGER, Hyperfine Interact. *32*, 589 (1986).
[58] G. KANELLIS, W. KRESS, and H. BILZ, Phys. Rev. B *33*, 8724 (1986).